Quantification of localized strains induced within a granular medium by a bi-phasic flow via digital image correlation

Rana Al Nemer, Julien Réthoré, Giulio Sciarra

Received: Added at production | Revised: Added at production | Accepted: Added at production

DOI: xxx/xxxx

FULL PAPER

Quantification of localized strains induced within a granular medium by a bi-phasic flow via digital image correlation

Rana Al Nemer* | Julien Réthoré | Giulio Sciarra

Nantes Université, Ecole Centrale Nantes, CNRS, GeM, UMR 6183, F-44000 Nantes, France

Correspondence
Rana Al Nemer, Nantes Université, Ecole Centrale Nantes, CNRS, GeM, UMR 6183, F-44000 Nantes, France
Email: rana.al-nemer@ec-nantes.fr

Summary

Bi-phasic flow propagating through a granular medium can be established as an unstable infiltration and can be precursors of non-negligible deformations. Capturing such infiltration through the lens of a high resolution camera, full-field strain maps are determined via digital image correlation. However, this image analysis technique is based on the fundamental assumption of gray level conservation between the reference and deformed images. In this paper, DIC algorithm is recalled and suitable controlling parameters are introduced to improve the accuracy of the output displacement fields and to remove the gray level variations induced by an air-water flow percolating through a Fontainebleau sand. In addition, an in-depth investigation on the full-field volumetric strain maps is conducted in order to extract the hidden relationship between the front propagation and the strains evolution.

KEYWORDS:
localized strains, bi-phasic flow, granular medium, digital image correlation

1 | INTRODUCTION

Geo-materials, either fine or coarse materials, are the basic constructive material of many engineering infrastructures such as dams, tunnels, offshore installations and geological storage. Particularly, understanding their behavior against hydro-mechanical loadings is fundamental to avoid catastrophic failures. Obvious examples of this complex coupling are ubiquitous in geotechnical engineering, from soil liquefaction, inducing slope instability, to internal erosion triggering different failure mechanisms in earth dams. In the following we shall focus in particular on geological storage applications such as CO_2 sequestration and temporal underground storage of methane or hydrogen, where in all these cases a pressure or flow controlled gas percolation through an initially saturated geo-material at a certain depth below the Earth's crust, can induce local deformation.

At laboratory scale, researchers have deeply studied the macroscopic deformation of geo-materials under axial and/or shear forces applied either on dry or saturated samples. However, thanks to the technology development and especially imaging technology, the measurement precision has now significantly improved so that a transition from a global average to contactless full-field measurement can nowadays be carried out. This progress has reflected on geomechanics domain [1,2] and many studies have been performed based on two-dimensional measurements using one digital camera [3], stereovision measurements using two digital cameras [4] and three-dimensional measurements using X-ray tomography [5,6]. The assessment of the acquired data is achieved via robust image analysis algorithms such as Digital Image Correlation (DIC) for 2D images and Digital Volume Correlation (DVC) for 3D images allowing to retrieve local information going from macroscale to microscale, depending on the spatial resolution of optical systems. So a solid matrix, having its own speckle or having been treated in order to get an artificial one can be monitored at different stages of loading, normally a mechanical one, and consequently a full-field measure

of the displacement field can be obtained after matching the acquired images between the reference and deformed states ([7]). In geomechanics, in particular, DIC and DVC are typically used for the monitoring of the dessication crack propagation in argillaceous rock [8], and the characterization of strain localization in sandstone [9], argillite rocks [5] or in granular material [10], when subjected to mechanical loadings. In our context, a new mechanism of deformation of geo-materials is questioned: the deformation induced by fluid infiltration through the porous skeleton.

Full-field measurements based on DIC are particularly interesting in the analysis of a mainly 2D phenomenon with respect to classical measure obtained by external transducers, typically adopted in standard biaxial [11] and triaxial [12] tests, which only capture the average response of the material. This is true in particular in the presence of a bi-phasic flow through granular media, which can turn into an unstable percolation, fluid fingering, depending on the physical properties of the two fluids and on the injection flow [13]. Consequently, aiming to characterize these preferential pathways and the subsequent skeleton remodeling, the contactless full-field measurement technique provided by DIC is undoubtedly the perfect candidate.

Most of the research works investigating the bi-phasic flow into a porous medium, have mainly focused on the immiscible fluid flow within a 2D Hele-Shaw cell – a cell constitued of two parallel transparent plates separated by a certain gap, possibly enclosing one layer of glass beads materials – and on the tracking of the displacement pattern [14–17]. Only few studies have tackled the coupling between fluid flow and the corresponding response of the percolated medium. For example, the work of Campbell et al.[18] sheds the light on the fracturing process induced by gas injection, of a water-saturated granular medium confined into a Hele-Shaw cell with one open end. The displacement of the glass beads, quantified by Particle Imaging Velocimetry (PIV), describes the opening of the medium. Another example conducted by Eriksen et al. [19] reports the interaction between fluid flow and the skeleton deformation, occurring also within a Hele-Shaw cell and due to a point-wise radial air injection. In [19], DIC is the technique used to extract the volumetric strain maps where positive volumetric strain indicating the dilation of the medium has been detected within the invaded zone. Regardless that no information has been provided neither on the DIC process nor on the handling of the artefact produced by the change of contrast through the drainage process, unstable percolation described by fluid fingering seems to be responsible of the generation of localized deformation with dilative behaviour. In addition, other studies focused on conducting drainage experiments on 3D sample, by percolating the gas (CO_2 for instance) into a brine-saturated shale sample conserving the in-situ conditions and similar conclusion regarding the deformation of the sample provided by macroscopic measurement is deduced [20,21].

One of the main interest of our study is the full characterization of possible deformations of the granular material induced by fingered (unstable) percolation of a gas (air) through an initially (water) saturated sand. According to the preliminary findings from the literature, there is still a lack of quantitative local information correlated to the tracking of the interface and the conditions which characterize the triggering of the unstable flow. In addition, to our knowledge, this is the first application of 2D-DIC to granular material subjected to 2D hydro-mechanical loading.

In the sequel, this paper is organized as follows: the experimental setup consisting on a new biaxial machine adapted to partially saturated medium is briefly described in Section 2, along with a reliable acquisition system to capture the unstable percolation. Then, the DIC algorithm is recalled in Section 3 with the gray level correction to remedy the change of contrast induced by fluid percolation. In Section 4, the spatial resolution is determined and the uncertainties of the measurement are quantified. Section 5 is devoted to the reveal of full-field volumetric strain maps and to the extraction of the hidden information from the full-field strain maps. In the last section, conclusions are briefly summarized.

2 | EXPERIMENTAL SETUP

2.1 | Biaxial machine for drainage experiments

As described by Chevalier et al. [22], drainage fingers are generated from the destabilisation of an homogeneous flat interface separating a non-wetting fluid (e.g. air) from a wetting one (e.g. water) moving within a Hele-Shaw cell [23] or a porous/granular matrix. To capture these hydraulic instabilities, and understand their impact on the matrix deformation, a biaxial machine adapted to unsaturated porous media has been designed and equiped with a high resolution optical system (see Section 2.2). This apparatus allows to control, simultaneously and separately, the confining pressure applied to the sample, as well as the pressures of the two fluid phases: the one of the wetting fluid, initially saturating the sample, and that of the non-wetting fluid injected to generate the drainage process. A schematic mainly focusing on the sample cell, its downstream and upstream connections, is presented in Figure 1, along with a photograph of the sample cell. A prismatic specimen of 50 mm height, 40 mm width and 11 mm thickness, is filled with Fontainebleau sand NE 34 of mean diameter d_{50} =210 µm, using the raining method that provides

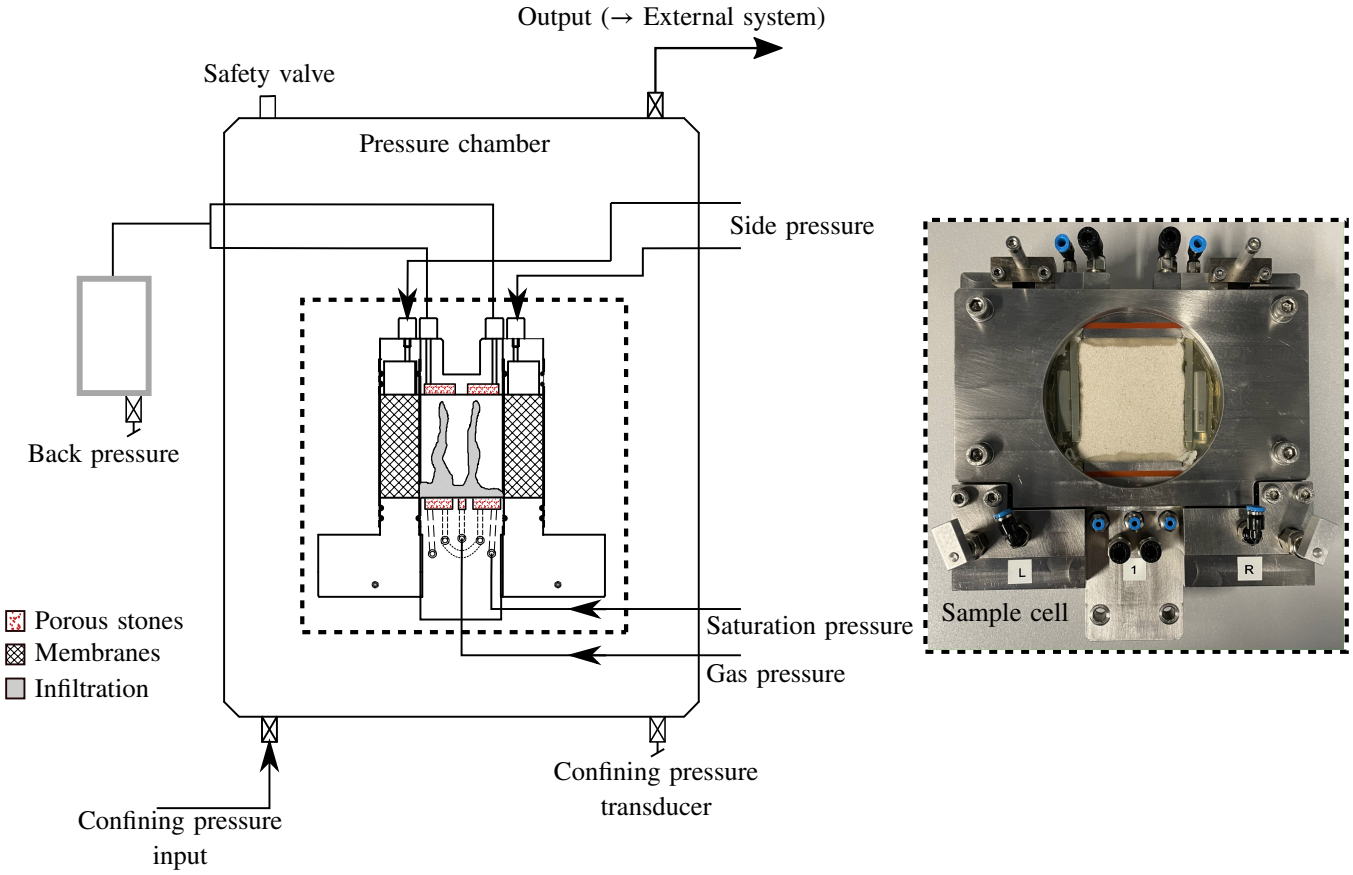

Figure 1 Schematic showing the pressure chamber, the sample cell and some connections on the left and a photograph of the sample cell on the right.

a uniform sand distribution. The largest sides are in contact with two transparent sapphire windows to promote the access to a scratch-free surface of the sample and to guarantee high quality images. The lateral sides are in contact with two latex membranes which allow to control the mechanical confinement while the top and bottom of the sample are in contact with the porous stones through which the pressures of the two phases are controlled.

After fixing the sample cell inside the pressure chamber, an initial confining pressure of 50 kPa is applied to the sample. It acts vertically on the free-top of the cell and horizontally along the longitudinal borders of the specimen via the circuit formed by the Pressure chamber-External system-Lateral membranes; this lateral pressure is referred on Figure 1 as side pressure. The water reservoir is then connected to the bottom porous stone and delivers water to saturate the medium due to a small gradient of pressure with respect to the upstream open to the atmosphere. To improve the saturation, the Skempton approach [24] is followed. A sequence of stepwise increments of confining stress (in undrained conditions) and back pressure is applied in order to maintain small effective stress, until complete saturation. At the end of the Skempton phase, the confining pressure and the pore water pressure which is determined from the last level of the back pressure are labelled as σ_{c0} and P_{p_0} respectively. Switching to drained conditions, an increase of the confining pressure $\Delta\sigma_c$ is then applied to boost the initial effective stress $\sigma_0^{'} = (\sigma_{c0} - P_{p_0)} + \Delta\sigma_c$, prior to the injection phase. Then the gas source (air) is connected to the base porous stone and air invasion is triggered by putting the gas at a pressure P_g that exceeds the defending water pressure P_{p_0}. This difference of pressure between the non-wetting phase (air) and the wetting phase (water) is called as capillary pressure. During the gas infiltration, the optical system presented in Section 2.2 films the process at a frequency of 30 Hz. For more details on the apparatus functioning and procedure of drainage test, we refer to Al Nemer et al. [25].

2.2 | High resolution optical system

The optical system associated to the biaxial machine is presented in Figure 2a and summarized in Table 1. Constituted by a high resolution 50 MPx camera (VC-50MX) mounted with a telecentric lens of magnification 0.75, this system records the infiltration process at a resolution of 6.1 µm/pixel and a frequency of 30 Hz. The field of view of (6004×7904 pixels^2) covers almost the overall surface of the sample (36.6×48.2 mm^2). The mounted setup is screwed on micrometric plates as pointed on Figure 2b, allowing to (i) center automatically the camera's sensor on the specimen surface by controlling the positions along the x and y axis and (ii) to adjust the focus by manipulating the z axis. In addition, a control of the rotation along z axis is possible to calibrate the perpendicularity of the optical system with the sample cell. The lighting system consists of two LED spotlights, covered by polarizing filters, to illuminate the target object without glare effect. The whole system, the optical one and the biaxial machine, is positioned on an optical table to avoid the vibrations effect (see Figure 2b). As mentioned in Section 2, the sample cell is characterized by a couple of transparent windows in contact with the specimen surfaces. The pressure chamber in which the sample cell is enclosed is also characterized by a couple of see-through porthole. Figure 2c shows from one-side view the parallel internal and external windows aligned with the telecentric lens.

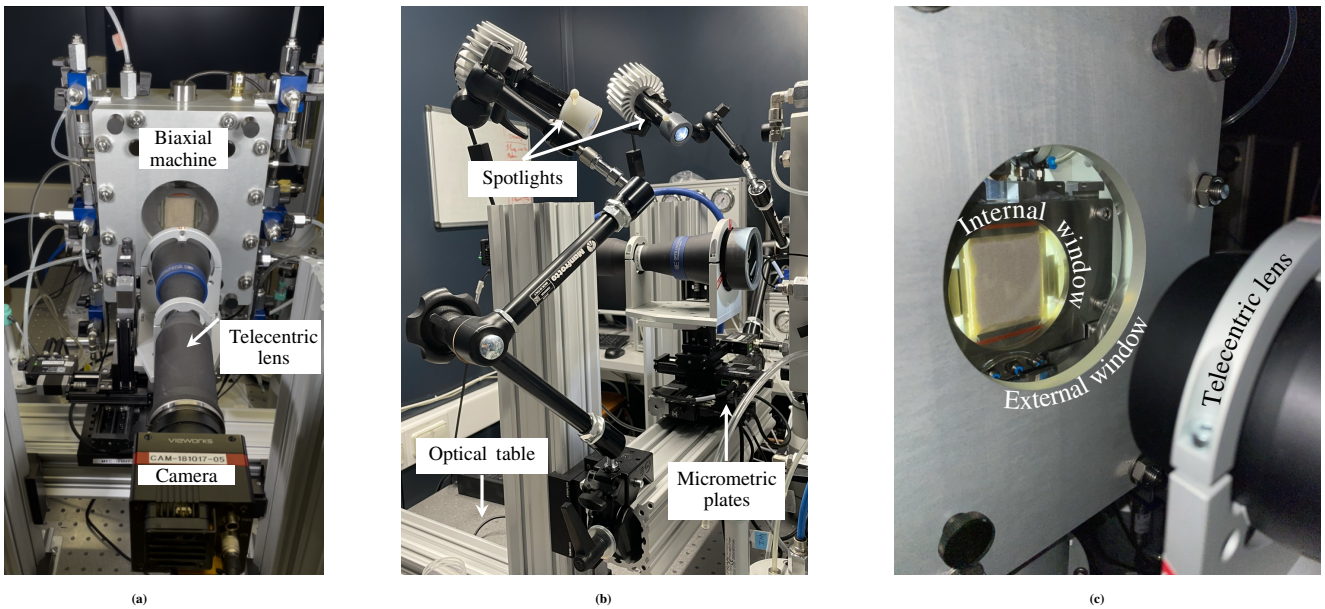

Figure 2 (a) Biaxial machine endowed with its optical system, (b) photograph showing the additional elements to the acquisition setup, (c) close up on the biaxial machine highlighting the internal/external windows from one-side view.

Camera	Lens	Resolution	Acquisition frequency	Field of view
VC-50MX	Telecentric of magnification 0.75	6.1 µm/pixel	30 Hz	6004×7904 pixels^2

Table 1 Characteristics of the optical system.

This duo composed of the bi-axial machine and the high-resolution optical system has allowed to monitor and track the infiltration of air through the saturated sand during the drainage process. The raw images acquired via the lens of the optical system at the breakthrough time t_b– the time at which the air reached the top of the sample – are presented in Figure 3 for three tests that have in common the capillary pressure of 30 kPa but differentiate in the initial effective stress ($\sigma'_{0(1)} = \sigma'_{0(2)} = 120$ kPa

Figure 3 Images of (6004×7904 pixels^2) acquired at the breakthrough time of three different drainage tests.

while $\sigma'_{0(3)} = 40$ kPa). It's worth to mention that the scope of this article is not to tackle the effect of the mechanical loading on the response of the medium but the effect of the unstable infiltration on the subsequent deformation.

3 | FE-DIC FORMULATION

3.1 | Basic principles

The granular soil material, Fontainebleau sand, has its own natural speckle. According to its grain size distribution, the grain diameter can vary from 150 µm to 300 µm. Therefore, using the optical system described in Section 2.2, each grain is represented by 25 to 50 pixels. When water-saturated sand is invaded by air, this last percolates through the porous network, and is expected to discard the grains from each other and in turn tightens the adjacent pores; a similar behavior is illustrated in Campbell et al. [18] and Chevalier et al. [22]. DIC is chosen to provide the full-field measure of the rearrangement of grains during fluid flow. A recall of the Finite-Element DIC (FE-DIC) is presented below.

DIC method allows to identify the displacement field that matches a deformed state to its reference one, based on the optical flow equation described by:

$$f(x) = g\big(x + u(x)\big) \tag{1}$$

which assumes that the gray level for each pixel at coordinates x in the reference image f is conserved and found at $(x+u)$ in the deformed image g, with u being the displacement vector at position x. However, Equation (1) describes an ill-posed non-linear problem since one equation is written at each pixel but two underlying displacement components are sought and u comes as an argument of g.

Through an iterative solution algorithm, the non-linearity in Equation (1) is disposed using a first order Taylor development, by assuming an infinitesimal displacement correction $du(x)$ from one iteration to the next one:

$$g\big(x + u(x) + du(x)\big) = g\big(x + u(x)\big) + du(x).\nabla g\big(x + u(x)\big) \tag{2}$$

where ∇ denotes the vector gradient operator. Then, to reduce the number of unknowns, a finite element discretization of the displacement field is adopted [26], as follows:

$$u(x) = \sum_{i\in\mathcal{N}} N_i(x)\bar{u}_i \quad \text{and} \quad du(x) = \sum_{i\in\mathcal{N}} N_i(x)d\bar{u}_i \tag{3}$$

where $\bar{u}_i$ and $d\bar{u}_i$ denote respectively the nodal displacement vector and its infinitesimal correction at the node i, N_i is the i^{th} shape function of the functional space adapted to the i^{th} node in the spirit of finite element method, and $\mathcal{N}$ is the total number of nodes of the finite element mesh defined within the frame of the Region Of Interest (ROI). Considering Equation (2) and Equation (3) with Equation (1) and gathering for all the pixels inside the finite element mesh, the matricial form is written as follows:

$$\{F - G\} = [\nabla_X G][N]\{d\bar{U}_X\} + [\nabla_Y G][N]\{d\bar{U}_Y\} \tag{4}$$

where $\{F-G\}$ is a vector that contains the residuals $f(x) - g\big(x + u(x)\big)$ evaluated at each pixel, $[\nabla_X G]$, respectively $[\nabla_Y G]$, is a diagonal matrix collecting the values $\nabla_X g\big(x + u(x)\big)$ the X component of the gray level vector gradient, respectively $\nabla_Y g\big(x + u(x)\big)$ for the Y component, and $[N]$ is a matrix in which each column reports the values of one of the basis functions at each pixel of the ROI. $[N]$ has as many rows as the total number of pixels within the ROI, N_p, and as many columns as the total number of nodes $\mathcal{N}$.

Equation (4) can be rewritten as follow:

$$\{F - G\} = \begin{bmatrix}[\nabla_X G][N] & [\nabla_Y G][N]\end{bmatrix} \begin{Bmatrix} d\bar{U}_X \\ d\bar{U}_Y \end{Bmatrix} \tag{5}$$

and consequently the sought vector $\{d\bar{U}\} = \{d\bar{U}_X \quad d\bar{U}_Y\}^T$, collecting the components of the displacement vector at all the nodes of the finite element mesh, is obtained by solving this over-determined system in a least-squares sense. After some manipulations, the linear system to be solved becomes:

$$[M]\{d\bar{U}\} = \{b\} \tag{6}$$

with

$$[M] = \begin{bmatrix} [N]^T[\nabla_X F][\nabla_X F][N] & [N]^T[\nabla_X F][\nabla_Y F][N] \\ [N]^T[\nabla_Y F][\nabla_X F][N] & [N]^T[\nabla_Y F][\nabla_Y F][N] \end{bmatrix} \tag{7}$$

and

$$\{b\} = \begin{Bmatrix} [N]^T[\nabla_X F]\{F - G\} \\ [N]^T[\nabla_Y F]\{F - G\} \end{Bmatrix}. \tag{8}$$

It is worth to underline that to optimize the computational cost by computing once for all the matrix $[M]$ and part of the vector $\{b\}$, ∇G is replaced by ∇F in Equation (7) and Equation (8) (for more details and alternative implementations, see Passieux and Bouclier [27]).

Note also that the over-determined system (4) made of N_p equations and $2\mathcal{N}$ unknowns has led to the use of the pseudo inverse of this system, namely:

$$\begin{bmatrix} [N]^T[\nabla_X F][\nabla_X F][N] & [N]^T[\nabla_X F][\nabla_Y F][N] \\ [N]^T[\nabla_Y F][\nabla_X F][N] & [N]^T[\nabla_Y F][\nabla_Y F][N] \end{bmatrix}^{-1} \begin{bmatrix} [N]^T[\nabla_X F] \\ [N]^T[\nabla_Y F] \end{bmatrix}. \tag{9}$$

Formally, this is equivalent to solving Equation (2) as a least-squares minimization problem:

$$\left(d\bar{u}_i\right)_{i\in\mathcal{N}} = \text{Arg Min} \sum_{ROI} \left[\begin{array}{c} f(x) - g\left(x + u(x)\right) - \\ \left(\sum_{i\in\mathcal{N}} N_i(x) d\bar{u}_i \right) . \nabla g\left(x + u(x)\right) \end{array} \right]^2. \tag{10}$$

As mentionned earlier, the solution of this problem is achieved via an iterative process: an initial nodal displacement vector $\{\bar{U}_0\}$ is assumed then $\{d\bar{U}\}$ is calculated based on Equation (6) and the nodal displacement vector $\{\bar{U}\}$ is updated. This process stops once the convergence criterion is satisfied; in our case when the L_2 norm of $\{d\bar{U}\}$ relative to the L_2 norm of $\{\bar{U}\}$ becomes lower or equal to 10^{-3}. The final output from this computation is the vector $\{\bar{U}\}$ collecting the nodal displacement vector $\bar{u}$. Then, the displacement vector u map that will describe the displacement of all the pixels falling within the ROI is obtained using Equation (3).

UFreckles [28], an open source software based on the FE approach described above, is used for DIC calculation. A FE regular mesh with square four-noded elements is generated over a ROI in the reference configuration. In the considered problem, air invasion induces a change of contrast between the reference and the deformed images and thus results into questionning the central hypothesis of DIC, say the gray level conservation. In the following, a way to overcome the gray level change attributed to gas injection is presented, in addition to the selection of the appropriate mesh size ensuring an accurate description of grain rearrangement.

3.2 | Gray level correction

Optical flow disturbance has been studied in the literature for various cases such as infrared images acquired during high-temperature tests [29], images acquired from two different imaging systems [30] and images acquired during crack growth [31]. Air infiltration through a water saturated granular medium introduces a new source of gray level change between the images shot at different times. Phase coexistence in the sample contributes to the brightening of the invaded zone and so to the change in contrast and brightness between the reference and deformed states. However, the central hypothesis in DIC is the gray level conservation so any change of contrast and/or brightness violates this assumption, if not corrected.

Gray level correction has been discussed initially for the local DIC by Sutton et al. [7], by introducing the zero-mean normalised sum of squared difference (ZNSSD) optimisation criterion. For FE-DIC, a second minimization problem integrated within the main one can be adopted to minimize the least-squares residual, based on Equation (1); the problem is solved iteratively in two stages: (i) for a fixed gray level correction fields, the residual functional is minimized to find the displacement u (see Equation (10)), (ii) for the calculated displacement u, another minimization problem is solved to tune the corrections corresponding to the brightness and the contrast [31]. Alternatively, instead of solving the double minimization problem and in order to remove the effect of gray level alteration due to the gas intrusion, we apply a "local" correction of gray level, done element by element, for each step of the iteration process that determines the value of the displacement vectors at the nodal points via Equation (6). In particular, the gray level of the deformed configuration g, is locally replaced by a corrected gray level $\tilde{g}$, using the following equation:

$$\tilde{g}(x + \tilde{u}) = \boldsymbol{C}(g(x + \tilde{u}) - \mu_{def}) + \boldsymbol{\mathcal{B}} \tag{11}$$

$\boldsymbol{C} = \sigma_{ref}/\sigma_{def}$, is the ratio of the standard deviations of the gray level within two corresponding elements in the reference and in the deformed image at the current iteration. The element in the deformed image corresponding to a given element in the reference configuration is identified, at each iteration, thanks to the displacement vector u. $\boldsymbol{\mathcal{B}} = \mu_{ref}$ is the mean value of gray level in the reference element, conversely μ_{def} is the mean value of gray level in the deformed element. Thus, Equation (11) allows to recover the gray level of the statistical distribution of the reference element, by changing the contrast of the deformed one via the term C and its brightness via the term $\mathcal{B}$. An example illustrating the case of gray level change induced by fluid

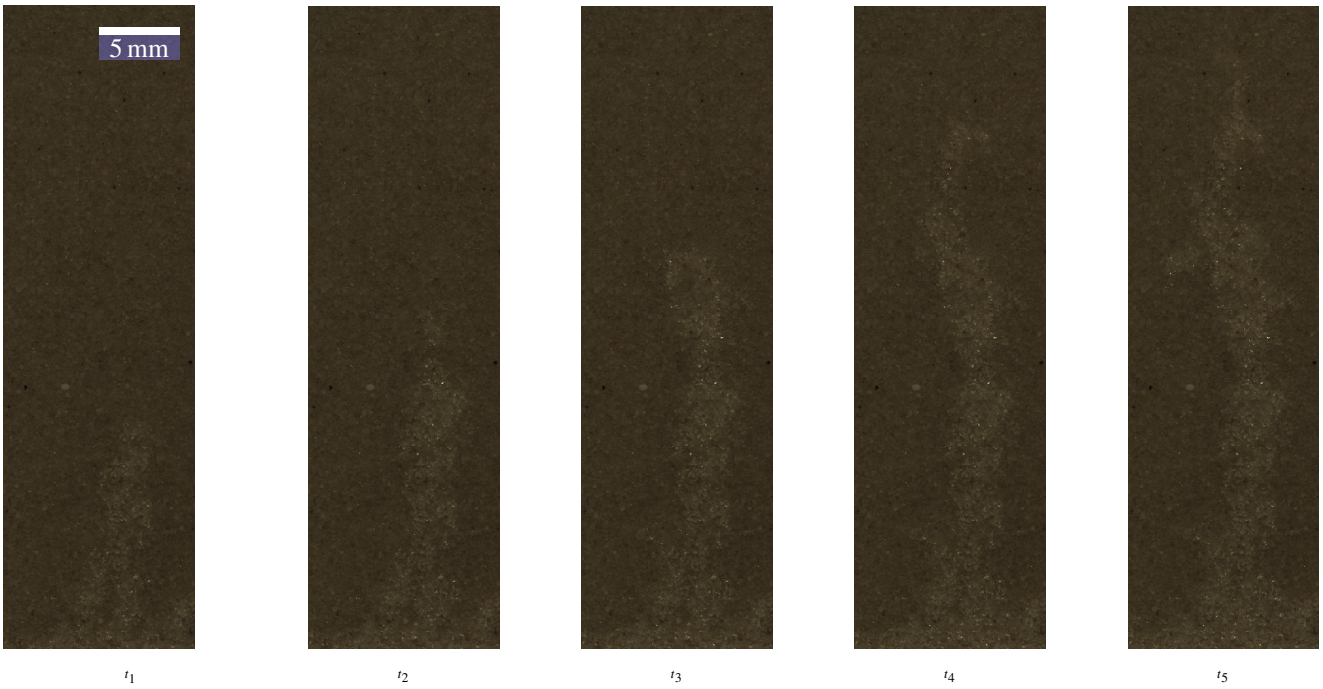

Figure 4 Raw images (1950 × 6600 pixels) captured during the drainage process: bright color represents the region invaded by air and dark color represents the region that remains saturated by water. The time-step between these images is 0.5s.

propagation, is presented in Figure 4. It consists on a sequence of images acquired during the drainage process when the air finger propagating from the bottom to the top in a water-saturated medium, alters the gray level locally. To emphasize the effect of the aforementioned gray level correction on the minimization process, the pixelwise residual map is calculated at a given time t, in two different ways and is represented: (i) in Figure 5a, as the difference between the gray level of a pixel in the reference image and its gray level in the deformed image but this latter being subjected to the gray level correction as per Equation (11), $\epsilon_{GL} = |f(x) - \tilde{g}(x + \tilde{u})|$ and (ii) in Figure 5b, as the difference between the raw data of gray level, $\epsilon_{GL} = |f(x) - g(x + \tilde{u})|$, without applying any type of gray level correction. Note that, for both cases, the displacement vector u that allows to correlate the deformed element to its corresponding reference element, is the one obtained from DIC calculation performed with local correction of gray level (referred as $\tilde{u}$ in Figure 5). We can clearly see how the local correction erases the fingerprint of the gas percolation and leads to an almost uniform residual map without any distinction between the invaded and intact zones. An additional validation of the adopted procedure is provided by the temporal evolution of the histograms of gray level residuals shown in Figure 6 for both cases. When local correction of gray level is applied, the histograms are superposed while the absence of gray correction generates a gap among the histograms relative to different time steps and higher values of residuals, as seen in Figure 6a. The same analysis is developed also considering only the invaded zone where the alteration of gray level has occured, see Figure 6b, in order to highlight the performance of the suggested approach into the targeted areas. The characteristic time steps used from now on wherever the time evolution of the drainage process is taken into account are $\{t_1, t_2, t_3, t_4, t_5\}$ depicted in Figure 4. Moreover the histograms of gray level residuals, in solid lines are spread out over at least 20 gray levels whereas they are more condensed over 5 gray levels when local correction is applied. So, the proposed gray level correction approach reduces significantly the artefact of contrast change and is essential for a better convergence.

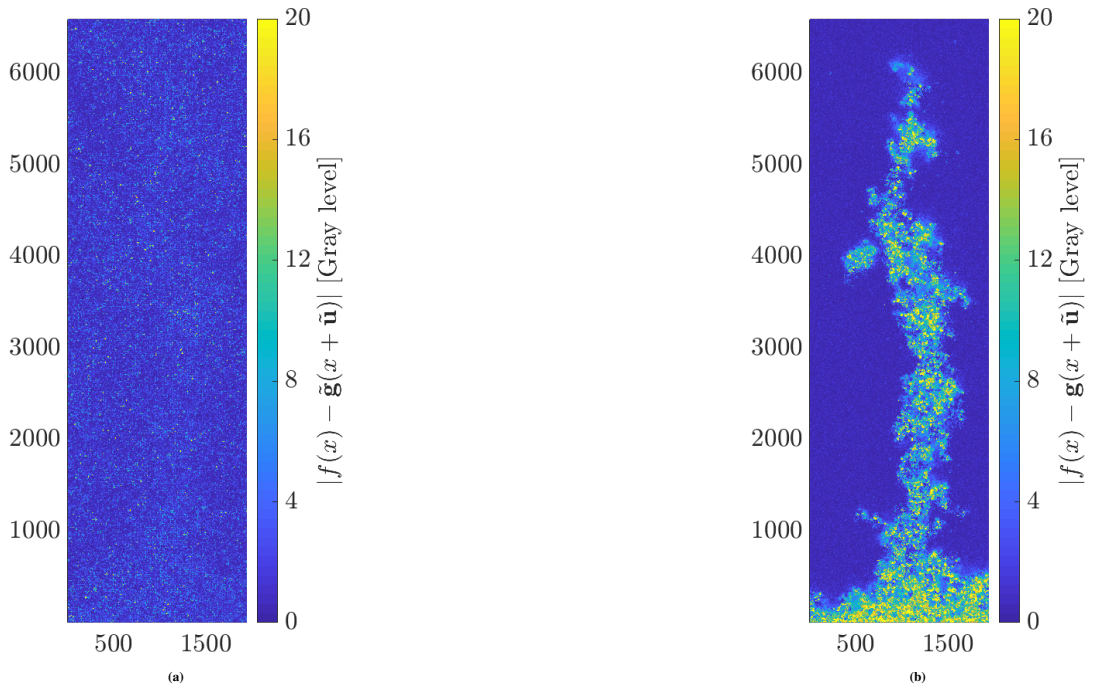

Figure 5 Pixel-residual error maps, in terms of gray level, for time t_5 shown in Figure 4, where local correction of gray level is applied in (a), whereas it is abandonned in (b). The displacement vector u is labelled here as $\tilde{u}$ to emphasize that in both cases is issued from the DIC calculation performed with local correction of gray level.

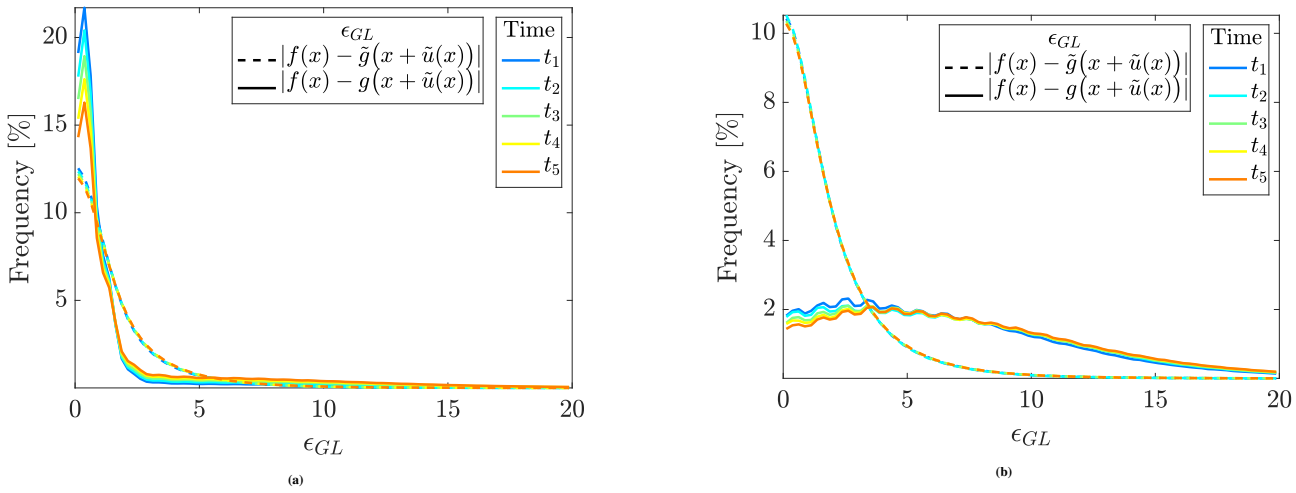

Figure 6 Histograms of gray level residuals for consecutive instants $t_{1\to5}$ acquired during the air invasion process and illustrated in Figure 4. Dashed lines indicate the gray level residual calculated considering the local correction while solid lines calculated with no correction. For both cases, the displacement vector $\tilde{u}$ is obtained from the same DIC calculation performed with local correction. In (a), the considered region is the ROI shown on the maps of Figure 5, whereas in (b) the considered region is only the invaded part.

4 | METROLOGICAL ANALAYSIS

4.1 | Spatial resolution

The characteristic size of the quadrilateral finite elements adopted to discretize Equation (1) is chosen on the basis of a qualitative comparison between the displacement field captured via DIC and the relative displacement of the two grains directly in contact with the transparent confining walls of the biaxial apparatus as observed by images in the first row of Figure 7 and estimated via ImageJ software [32]. Different mesh sizes have been tested, in particular M_{DIC}=5, 10, 20 pixels, on a sequence of windows of dimension 100×100 pixels extracted from the images of the drainage process at different time steps, see Figure 7. The local

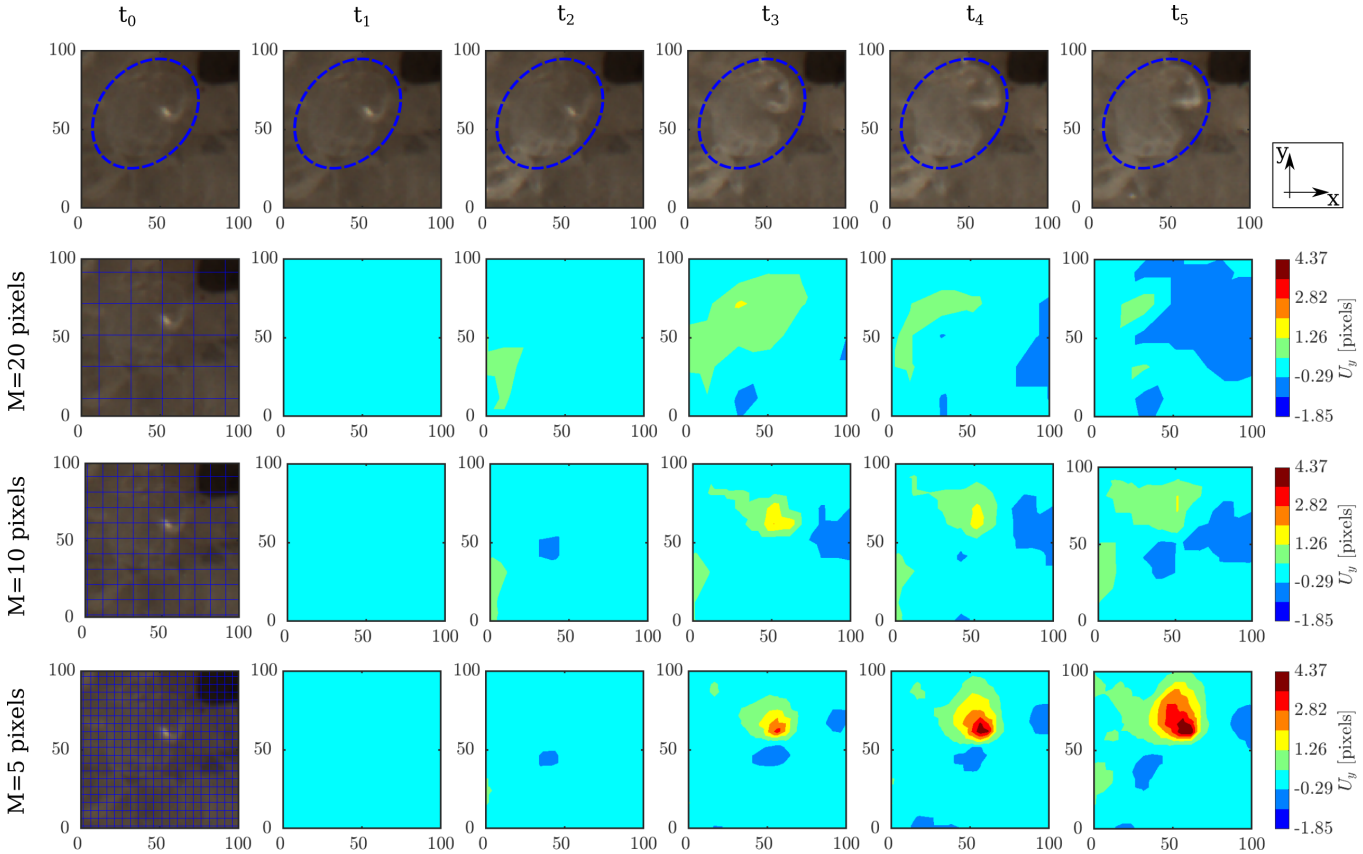

Figure 7 Time evolution for the vertical displacements U_y obtained from different mesh sizes (M=5, 10, 20 pixels) on a domain of 100×100 pixels. t_0 indicates the reference state and t_i $(i > 0)$ indicates the deformed state.

correction of gray level, detailed in Section 3.2 is applied; moreover, a Tikhonov regularization [33,34], that aims on filtering the displacements with a wavelength smaller than a cut-off wavelength λ of 15 pixels is used to filter out high frequency displacements obtained from the DIC analysis. An additional median filter is finally employed at each iteration of the solving algorithm. This filter allows for further removing aberrant values of the nodal displacement without increasing the cut-off wave length of the Tikhonov regularization, what may decrease the resolution of the measurement. It consists on substituting the nodal value of each displacement components by the median value from the first neighboring nodes (in the sense of the finite element mesh connectivity).

DIC calculation is launched for each mesh size, between the reference image t_0 and the deformed images $t_1 - t_5$ captured during the infiltration process. The results obtained from DIC in terms of vertical displacement U_y are represented in the reference configuration in Figure 7. They show that a coarse mesh size with 10 pixels element or more, is not able to detect grain rearrangement as observed all along the drainage process. However, a mesh size of 5 pixels is sensitive to grain displacements and properly captures the mutual separation of a couple of grains initially in contact, pointed by the blue dashed ellipse in the

first row of Figure 7; the measured values are also in the same range as the ones estimated by ImageJ software. This justification leads to the adoption of a 5 pixels mesh size as an input to the DIC calculation in order to achieve an accurate measurement of grain separation at the microscopic scale.

The flow lines of the displacement field, represented as a function of the current position rather than of the reference one, within the above mentioned observation squared window of size 100 pixels, are represented in Figure 8 (starting from t_3). Colors indicate the displacement magnitude U_{mag} and the length of the arrows is magnified by a factor of 3. Apparently the flow lines are consistent with the grain separation observed in the images and the displacement magnitude intensifies from one timeshot to another, describing the progressive discharge of grains caused by the air infiltration. Volumetric strain map presented in Figure 8, is smoothed by a median filter. It consists on replacing the strain value of one element by the median of the values in the neighboring elements; neighboring is here meant in the sens of the finite element connectivity: the neighboring elements are elements that have at least one of the nodes of the considered element in their connectivity. This filtering has no smoothing effect (it does not remove short wave length in the strain field), it only removes outliers and uncorrelated spatial noise. Calculated for the last time-step t_5, it shows that the opening of the granular medium is described by positive volumetric strains while the compaction of the adjacent zone is provided by negative volumetric strains.

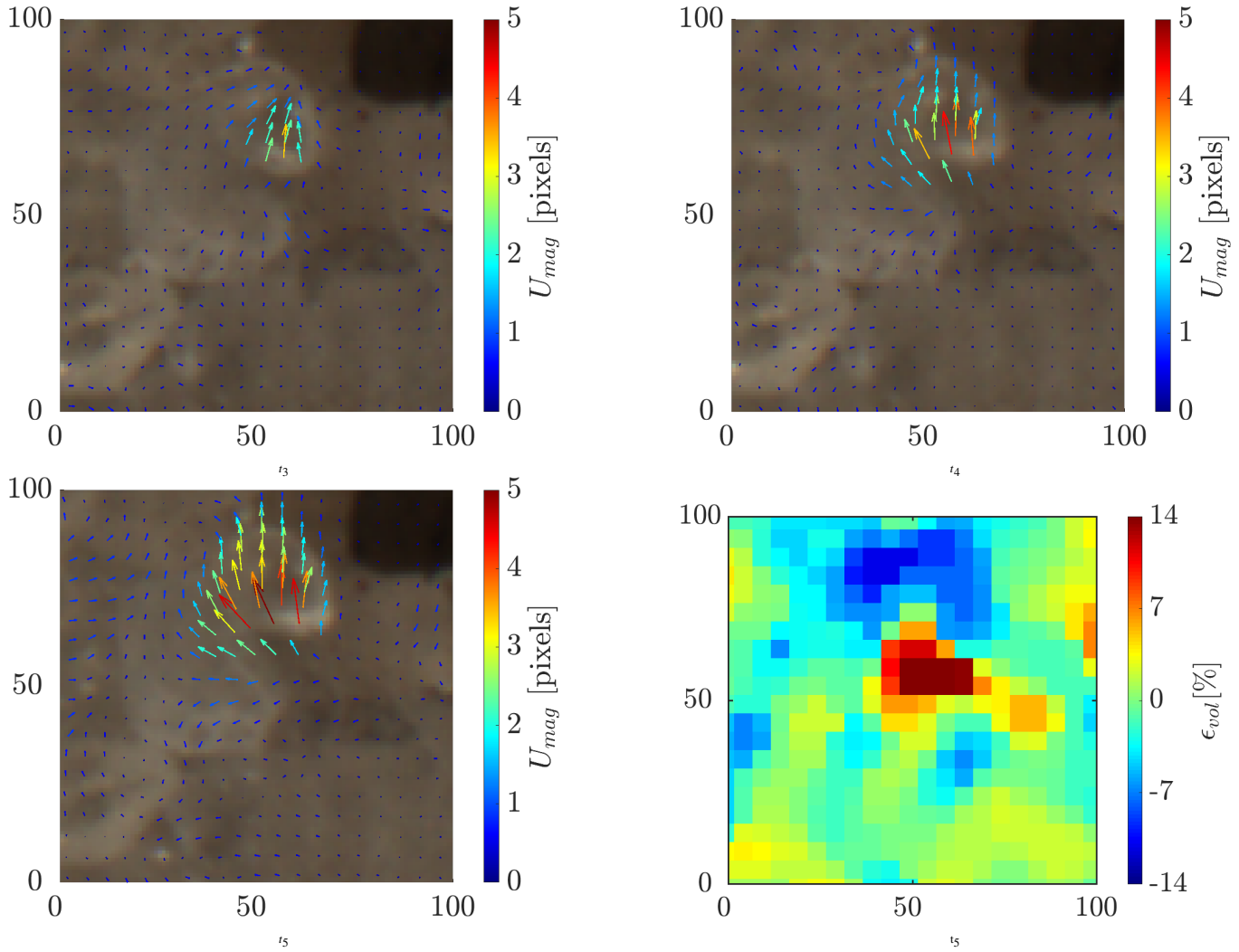

Figure 8 Eulerian representation of the displacement vector layered on top of the deformed images to confirm the granular motion. These vector fields are colored by the displacement magnitude U_{mag} and displayed with a magnificator of 3. The last map, the volumetric strain map ϵ_{vol} shows the positive and negative volumetric strains consistent with the opening and tightening of the granular medium, respectively.

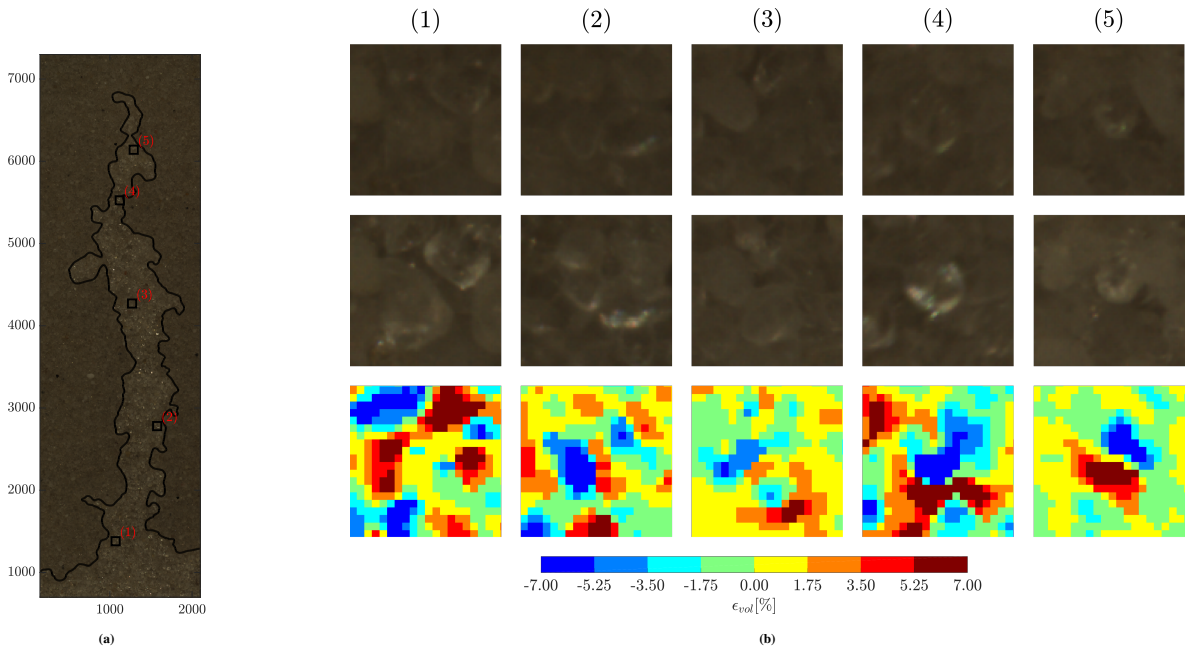

Figure 9 Scanning overall the finger the validity of the volumetric strain measurement, in Figure 9a the position of the elements tested and in Figure 9b, in the first row close up images of 100 × 100 pixels for each of the indicated position, shown in the reference configuration, the second row their deformed states and the last row the volumetric strain measurement by DIC.

A comparison between displacements directly observed by comparing insets of the image acquired at time t_5 with the reference state, and volumetric strains measured via DIC is reported in Figure 9. Different locations are identified where to put a control window of size 100 × 100 pixels. The chosen locations are shown in Figure 9a, their corresponding close up in the reference configuration in the first row of Figure 9b and their deformed states in the second row. The evaluated volumetric strains reported in the third row are consistent with the visual observation of opening and tightening of the porous space. This delivers an additional confirmation on the reliability of the 5 pixels fine mesh.

4.2 | Uncertainty measurements

The optical system chosen to survey the air infiltration into the sand medium is constitued by a high resolution camera of 50 MPx equiped with a telecentric lens (for more details, see Section 2.2). The visualization of the grains movement driven by the fluid percolation is going to be quantified via FE-DIC. So to extract the full-field motions, three elements have contributed: the specimen undergoing the infiltration, the optical system filming the process and the DIC algorithm processing the acquired images. Each element incorporate underlying uncertainty that will affect the accuracy of the measurement. The percolation of fluid generates a change of contrast, a sufficient source for the divergence of DIC algorithm, if not corrected. The optical system, intended to film the invasion process, adds some errors to the acquired images depending on the stability of the sensor. And finally, the DIC algorithm supplied by the acquired images and controlled by several inputs, can also be a source of measurement errors. Therefore, two tests called by “stability test” and “virtual change of contrast test” are addressed in the sequel to quantify possible errors induced by the above-cited sources.

It is to be noted that the conditions under which the drainage experiments are conducted and filmed, such as the polarized light, the acquisition frequency (30 Hz), the exposure time, and the (room) temperature are conserved in the following experiments dedicated to the quantification of the measurement errors and therefore the induced errors are strictly coming from the optical system, the specimen and the algorithm.

4.2.1 | Optical system uncertainty: stability test

The optical system on its own can be a source of errors and the typical way to estimate these errors, assigned to the sensor stability, resides in performing steady acquisition at the same acquisition frequency used in drainage experiments: a sequence of

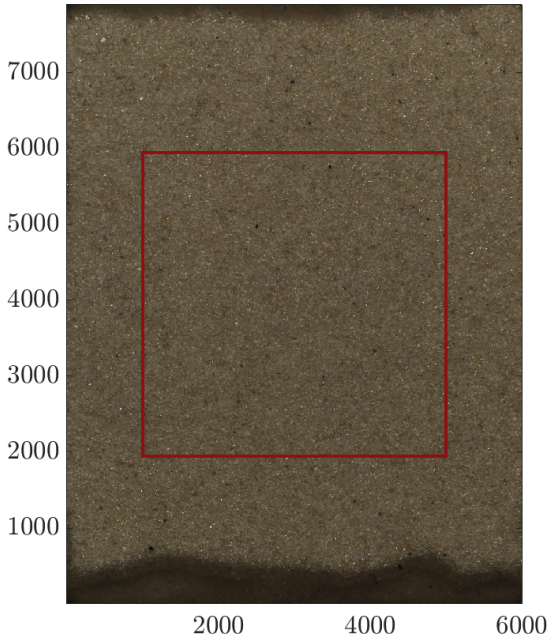

Figure 10 Centered zone delimited by the red border of 4000×4000 pixels over which DIC is executed.

images is acquired at a frequency of 30 Hz, over a period of 3s -longer than the duration of the conducted drainage experiments- for a fixed pattern of Fontainebleau sand. So a sample of Fontainebleau sand is placed inside the pressure chamber without applying any mechanical loading then filmed. The first acquired image is considered as the reference state and the remaining as the "deformed" states. Then, the DIC algorithm based on a finite element mesh of size 5 pixels, justified in Section 4.1, is applied to the group of acquired images over a centered ROI of (800×800) elements, that corresponds to 4000×4000 pixels as depicted in Figure 10. A zero displacement and consequently a zero deformation are expected since the filmed pattern does not undergo any loading.

The first invariant of the strain tensor, the volumetric strain, is one of the essential measurement to describe the response of the medium through a drainage experiment. Having here the displacement with only two non-vanishing components, volumetric strain is calculated as the trace of 2D strain tensor, $\epsilon_{vol} = \epsilon_{xx} + \epsilon_{yy}$, with ϵ_{xx} the horizontal strain and ϵ_{yy} the vertical strain. The strain values are represented by their average values over each finite element of the mesh. Then, the average value of this quantity is calculated for each "deformed" image acquired during the stability test at time t and according to two types of gray level correction: the global correction that relies on the gray level of the whole studied zone and the local correction that supplies the matching process with the element-wise gray level information (see Section 3.2). The evolution of the average value is reported in Figure 11 and the evolution of the standard deviation value is reported in Figure 12, as function of time. The calculated average values oscillate within the interval [-5 ; 7] $\times 10^{-4}$ %, indicating a negligible strain over the whole acquisition period, regardless the type of gray level correction. In parallel, the calculated standard deviations of the volumetric strain show a stable value all over the acquisition time but a lower value when local correction of gray level is admitted. One can conclude that local correction does not deteriorate the metrological performance of the method, even though in this case there is no change in gray levels due to particle movement or fluid invasion. The only variations in gray levels are due to the noise of the camera sensors and possibly to the vibrations of the experimental bench.

This DIC calculation being performed by considering a Tikhonov regularization, a parametric study is conducted on the cut-off wavelength λ. Then, the standard deviation of the volumetric strain, averaged over the set of the acquired images, is presented as function of λ in Figure 13a. As expected, whatever the regularization wavelength is, the local correction delivers lower measurement errors than the global correction. Moreover, the higher the cut-off wavelength is, the lower the uncertainty is, due to the smoothing effect brought by the regularization parameter. The cut-off wavelength to be used is usually recommended to be three times the size of the finite element mesh size; therefore a regularization of 15 pixels is endorsed. Considering a mesh size of 5 pixels while the characteristic size of the grains is around 35 pixels, a regularization with a cut-off wavelength of 15 pixels will allow to filter out the measurements at a scale smaller than that of the grain scale while our focus concerns the

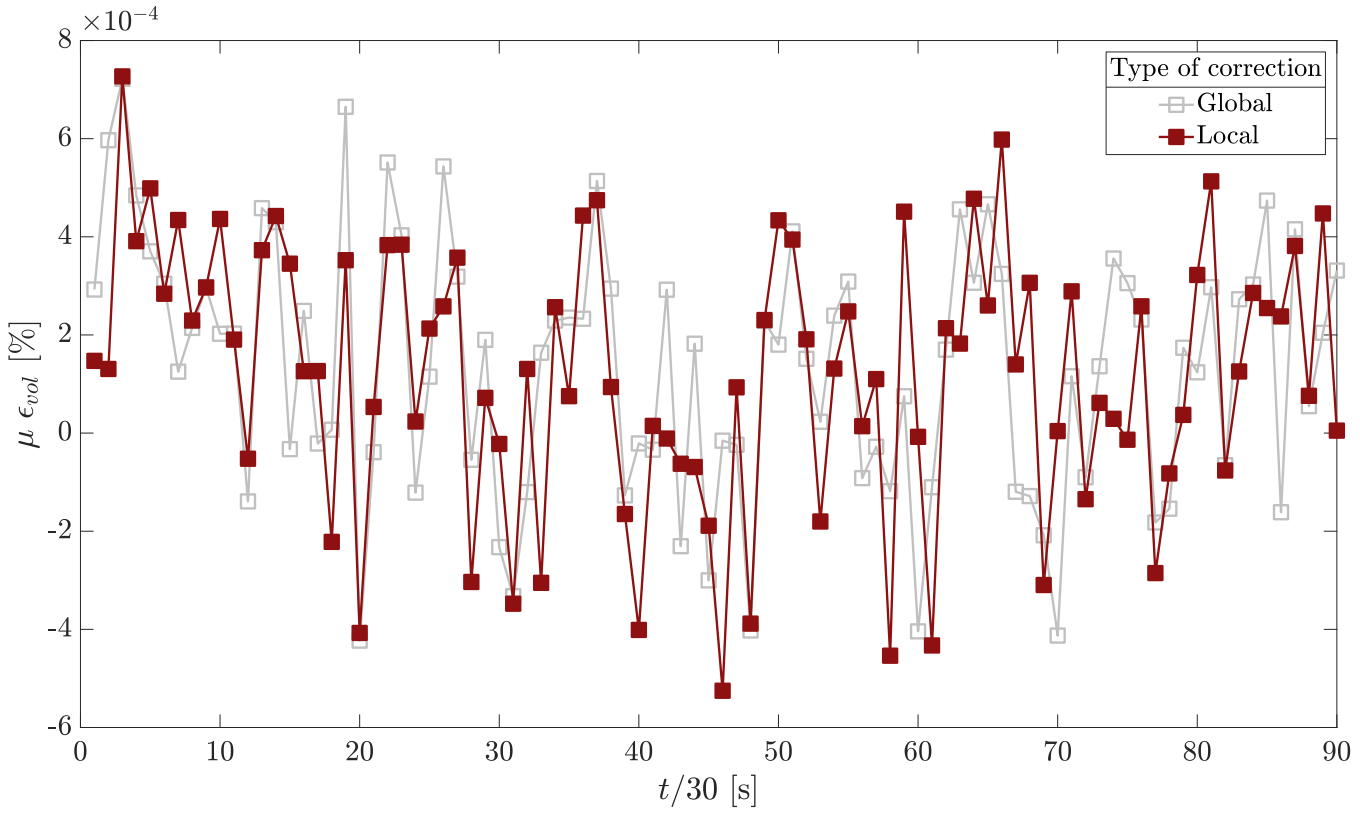

Figure 11 Evolution of the average value of the volumetric strain derived from DIC calculation with a Tikhonov regularization of 15 pixels and mesh size of 5 pixels and tested under two types of gray level correction, over an acquisition period of 3s.

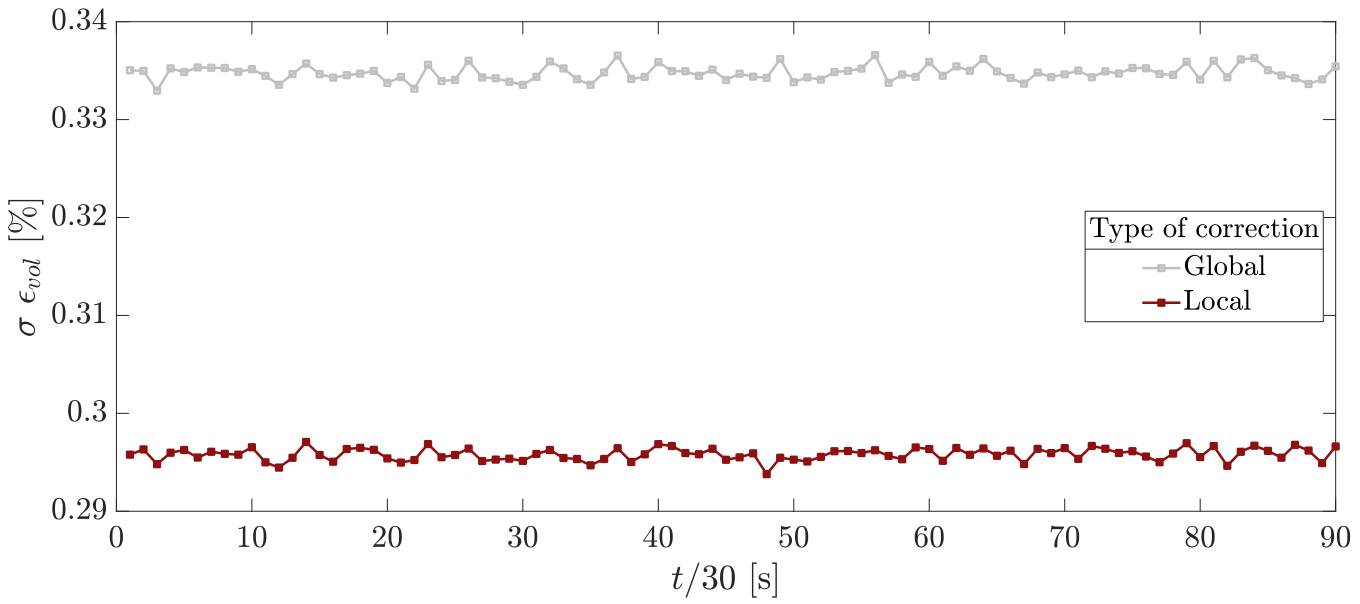

Figure 12 Evolution of the standard deviation value of the volumetric strain derived from DIC calculation with a Tikhonov regularization of 15 pixels and mesh size of 5 pixels and tested under two types of gray level correction, over an acquisition period of 3s.

Stability errors [%]	
ϵ_{vol}	J_2
0.2958	0.1101

Table 2 Summary of the induced errors due to the sensor stability on the first and second invariant of the strain tensor after the application of local correction of gray level and a Tikhonov regularization with $\lambda = 15$ pixels.

grains rearrangement. Therefore, this choice allows to measure the local arrangements in a resolute way (thanks to the 5 pixels elements), and robustly (thanks to the 15 pixels regularization). A similar analysis is conducted on the second invariant of the strain tensor J_2, the octahedral shear strain; the graphs are presented in Figure 13b. Same conclusion is again found regarding the closeness of the response following a local or global gray level correction. The measured uncertainties for the first and second invariant of the strain tensor are summarized in Table 2, for a $\lambda = 15$ pixels and local correction of gray level.

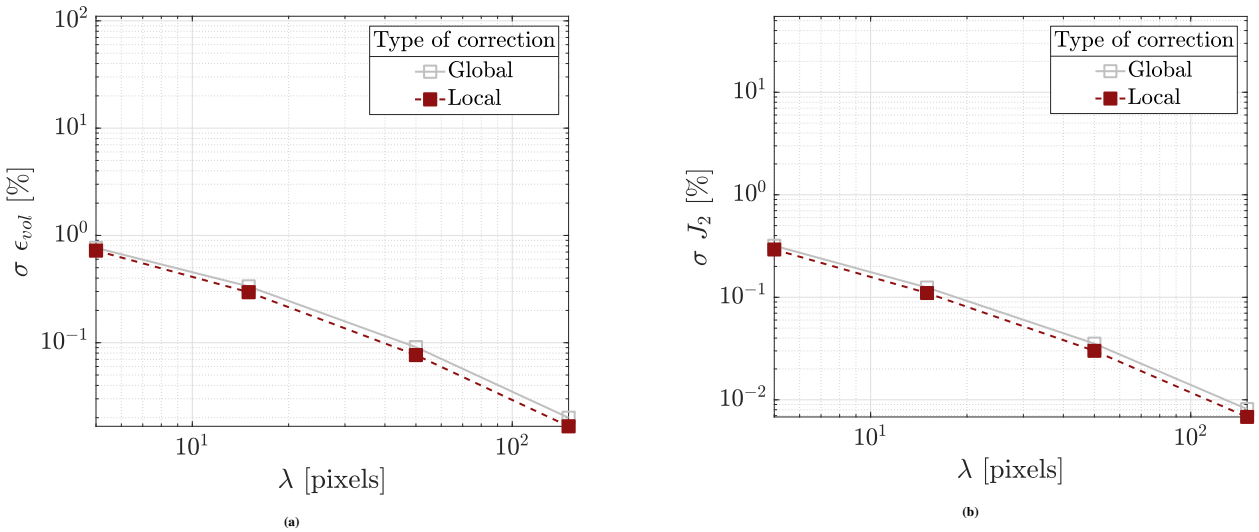

Figure 13 Evolution of the standard deviation of the first strain invariant in (a) and for the second strain invariant in (b) as function of the cut-off wavelength, using either a local or global correction of gray level in the DIC algorithm applied on the fixed images acquired during the stability test. The graphs are in logarithmic scale.

4.2.2 | Intrinsic uncertainty to bi-phasic flow experiment: virtual change of contrast test

When imaging system is set up to record the response of a structure or of a medium, the lighting intensity is normally controlled via external spotlights to avoid the environmental change of light. However, in many situations, uncontrollable effects emerge during the experiment, and alter the gray level information continuously, producing a significant change of contrast within the acquired image itself as well as with respect to the reference state. This problem can be encountered during a heating process of a material, a structure explosion, or a fluid percolation into a porous medium. During a drainage experiment, the air infiltration through the initially water-saturated sand, induces a change of contrast which will absolutely perturbate the iterative process of DIC, if not corrected. The local correction of gray level has proven to be a preferential approach capable to reduce the uncertainty measurements when no gray level change has occured. The question that naturally arises is to which extent the local correction approach is capable of fixing the situations where a gray level change occurs. To answer this question and quantify the measurement errors induced by the change of contrast, the gray level is modified in five images selected from the sequence of the "deformed" images acquired during the stability test, to simulate virtually the effect of the bi-phasic front propagation;

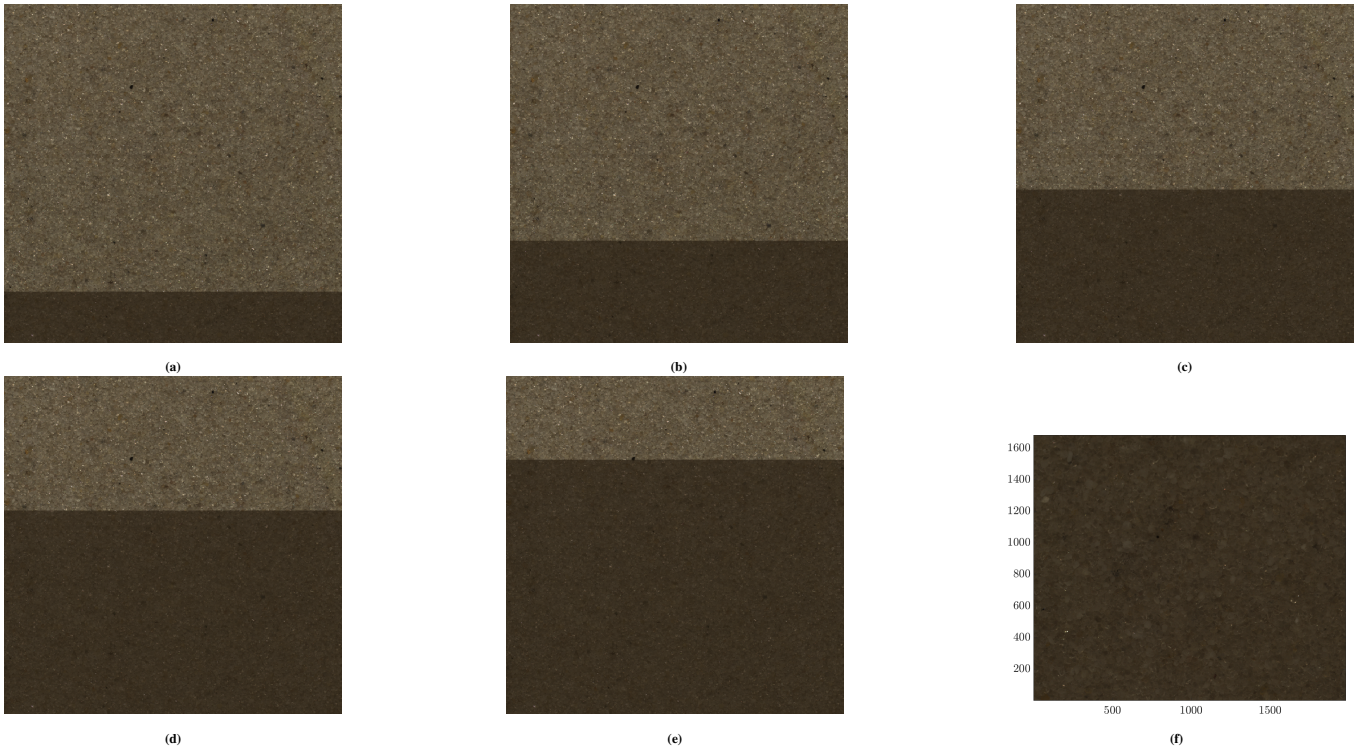

Figure 14 Sequence of 5 images (a-e) showing progressive zones with a gray level modified virtually, based on the raw gray level provided from a real fully water-saturated region as the one presented in Figure 14f. The virtually saturated zones illustrate the propagation of a virtual linear front into the dry sand. The size of the images is 4000×4000 pixels, issued from the same zone depicted in Figure 10.

the five virtually generated images are shown in Figure 14 (a-e), with a linear front propagation. This change of gray level transforming the dry state to virtually saturated one relies on the real average gray level identified after the full saturation of the medium by water; an example illustrating the full saturation of a medium is presented in Figure 14f. Similarly to Section 4.2.1, the DIC calculation is held over the whole domain with local correction of gray level from one side and with global gray level correction from the other side, to emphasize the benefit provided by the first type of correction. The standard deviations of the first and second invariant of the strain tensor, are first calculated at each timestep, only within the zone that has received the gray level change in the virtual images, then averaged over the 5 modified zones. The evolution of the averaged standard deviation is reported as function of the regularization parameter λ in Figure 15a and Figure 15b.

As expected, the local gray level correction leads to lower uncertainty compared to the global gray level correction and generates higher gap between the two responses compared to the result in Figure 13. Therefore, when an alteration of gray level is induced by a certain phenomenon, a local correction of gray level is very effective to compensate this undesirable gray level change. Moreover, the smoothening effect induced by the increase of the regularization parameter is replicated again. Table 3 sums up the residual uncertainty after the application of local gray level correction, using $\lambda = 15$ pixels. By comparing these values to the ones reported in Table 2, one can conclude that the local correction of gray level has almost completely erased the effect of change of contrast since the error measurement conducted on "virtual" test incorporates implicitly the ones previously quantified in "stability" test.

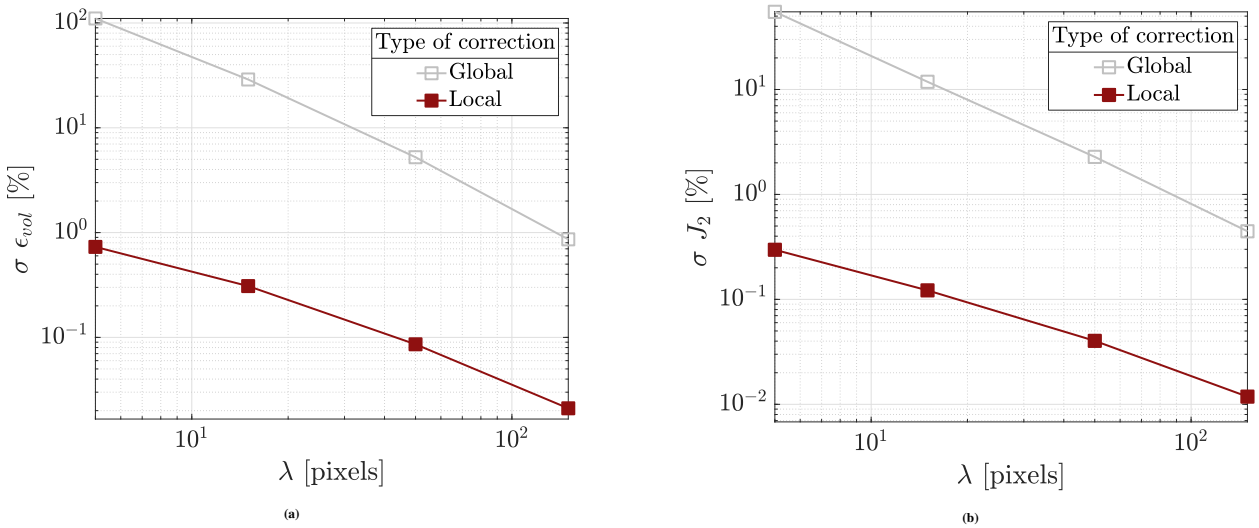

Figure 15 Evolution of the standard deviation of the first strain invariant in (a) and for the second strain invariant in (b) as function of the cut-off wavelength, using either a local or global correction of gray level in the DIC algorithm applied on the virtually saturated images. The graphs are in logarithmic scale.

Change of contrast errors [%]	
ϵ_{vol}	J_2
0.3088	0.1219

Table 3 Summary of the induced errors by the change of contrast on the first and second invariant of the strain tensor, after the application of local correction of gray level and a Tikhonov regularization with $\lambda = 15$ pixels.

5 | EXPERIMENTAL RESULTS

5.1 | Full-field volumetric strain maps

After verifying the mesh size to be used for the detection of the local grains rearrangement, underlying the importance of applying the local correction of gray level to reduce the artefact generated by the change of contrast and regularizing the displacement field by a 15 pixels cut-off wavelength, the FE-DIC approach is applied over an extended ROI covering each developed finger observed in the first three tests, for which the final states are illustrated in Figure 3. In Figure 16, the volumetric strain maps, regularized by the median filter already discussed in Section 4.1 and calculated at equally spaced instant of 0.5s during test (1) are presented. In addition, Figure 17 and Figure 18 show similar charts of the volumetric strain relative to test (2) within a zone including the finger and in test (3) in two separate regions including the two fingers which simultaneously progress in the sample, respectively. The time step in test (2) is 0.2s whereas in test (3) the time step is 0.1s and the maps presented for left finger correspond to the same instants as the right one. The black lines shown on all the volumetric strain maps separating the invaded zone from the non-invaded one, are obtained by segmenting the correlation residual map as that presented in Figure 5b.

One can notice that the progress of the fluid front generates narrow clusters of elements associated to positive and negative volumetric strains, in the drained zone of granular medium. The order of magnitude of the measured strains is clearly larger than the previously quantified errors whose signature can be seen in the non-invaded areas.

Given the characteristic size of the finite elements used to develop the FE-DIC analysis, these strain patterns reflect the displacements of the grains: in this spirit, local dilation corresponds to grains that are pushed apart from one another, giving rise to a looser configuration, and consequently positive volumetric strain; local shrinkage to densification of grains, say grain reorganization from an initial configuration towards a denser one, and consequently negative volumetric strain. These local

volumetric strains can be the consequences of local phenomena taking place at the pore scale level known as Haines jump events. A Haines jump event consists in a sharp drop of the capillary pressure when the gas enters in the target pore while the wetting fluid in the neighbor channels is driving forwards the non-wetting fluid. During drainage, the non-wetting phase infiltrates firstly the largest channel as, according to the Laplace law, this has the lowest entry pressure. When the meniscus passes from the pore neck into the pore, initially occupied by the wetting phase, the capillary pressure drops down because of the change in meniscus' curvature. Considering the classical definition of the Bishop effective stress, valid in the regime of partial saturation, say $\sigma' = \sigma + P_c S_r$ (here the convention of geomechanics assuming positive compressive stress holds true), the local effective stress drops down too, which explains the local expansion of the granular medium. Conversely the grains discarded by the gas flow, generate local compaction in the neighborhood channels.

Globally, the average volumetric strain calculated over the drainage process is positive for all the tests, indicating the dilation of the medium. For instance, the evolution of the average volumetric strain within the developed finger of test (2) is presented in Figure 19. This result of positive volumetric strain confirms that the global impact of the infiltration on the granular medium consists on the dilation of this latter. This observation has also been observed in other tests (1&3).

5.2 | From volumetric strain maps towards strains debriefing

The charts of the volumetric strain, as presented in Figure 17 and Figure 18, show the distribution of the strains within the developed finger and provide a global view over the order of magnitude of deformation. However, the sought correlation between the fluid flow and the localized strain is still missing. A deep investigation is therefore conducted to find out the underlying local information taking into account firstly the spatial distribution of the induced strains with respect to the progressive invaded zones and secondly the time history of the peak strain. In this section, only tests (2) and (3) are going to be analyzed.

5.2.1 | Zoned-strains description

In order to investigate the correlation between the progress of the gas front through the granular material and the appearance of local volumetric strains, DIC is applied to the study of the zones progressively invaded by the gas and those representing the complement of the invaded zone at time t_i with respect to that relative to time t_{i+1}. The invaded zone is therefore the whole drained region delimited by the current interface at a time t as depicted in Figure 20a and Figure 20b, whereas the transition zone is defined as the zone enclosed within two consecutive interfaces, as shown in Figure 20c.

Now, the set of elements corresponding to each invaded zone and to each transition zone being recognised, a local analysis is performed, zone per zone, to investigate in the evolution of the mean volumetric strains during the drainage process. In Figure 21a, the temporal history of the mean volumetric strains within each invaded zone, during test (2), is presented as function

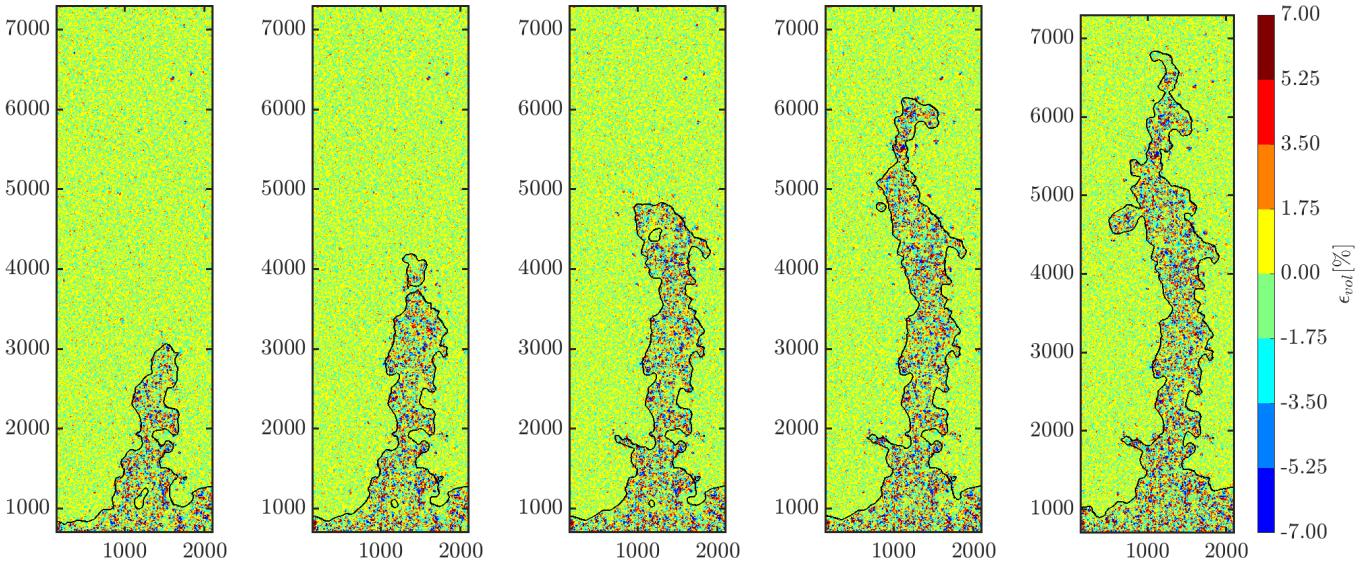

Figure 16 Volumetric strain maps for the single finger detected in test (1). The time-steps between the maps is 0.5s.

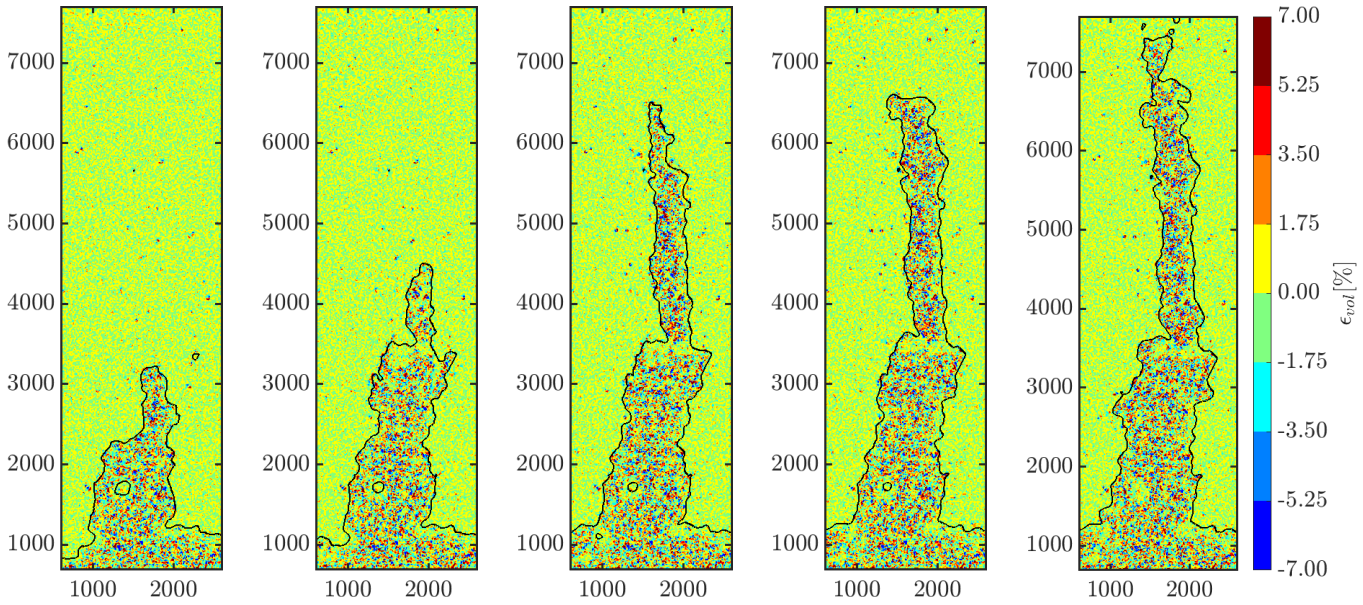

Figure 17 Volumetric strain maps for the single finger detected in test (2). The time-steps between the maps is 0.2s.

of the acquisition time normalised by the breakthrough time t_b of the corresponding test; the curve in dark blue corresponds to the first invaded zone located at the base of the finger whereas the one in dark red corresponds to the penultimate stage of the developed finger obtained in test (2). The solid lines denote the mean values of the positive volumetric strains while the dashed lines denote the mean values of the negative volumetric strains. This graph describes implicitely, the variations in the deformation of the elements within each invaded zone through the invasion process, reflecting the influence of the propagating interface on the previously generated invaded zones.

Focusing on the response of the average volumetric strain within an invaded zone, as for instance, the first one, the mean value of deformation is increasing at early stages of the invading process, until it reaches a constant value after a certain interval of time (around $t/t_b = 0.15$). This means that some elements within this zone have been undergoing fluctuations in deformation, impacting the global deformation, only over this short time interval, even though the air infiltration is still active. However, in the case of larger invaded zone reached at later time stages, a lighter increase in deformation at the beginning and a faster tendancy for stabilisation are established. This means that the more the finger is developing, the lower is the impact of the propagating interface on the global deformation or in other words, at later time stages, the progress of the interface is accompanied by a more complete desaturation of the invaded zones.

In addition, the larger the invaded zone is, the smaller the average volumetric strains are. By comparing the state of deformation within two consecutive invaded zones at the same time t, one can deduce that the average strain in the first zone usually remains higher than the one in the subsequent zone which means, that the new-deformed area enclosed within the last invaded zone, has a lower magnitude strain with respect to the average value reached within the former invaded zone. This is deduced given that an invading zone at a time t_{i+1} (Figure 20b) is the combination of the new transition zone (Figure 20c) with the previous invaded zone acquired at time t_i (Figure 20a).

A complementary investigation is given in Figure 21b, where the same averaging process is conducted but only within the transition zones. Figure 22 illustrates the sequence of transition zones observed in test (2) until the breakthrough occurs. The first value of each curve in Figure 21b reflects the average strain within the transition zone at the moment of its formation while the remaining part of each curve describes the influence of the fluid flow on the state of deformation of the transition zones once the front itself progresses far from the zone. One can deduce that the more new transition zones are generated, the more the effect of the invading process on the microstructure reorganisation is reduced, since the volumetric strain inside the new generated transition zones is globally decreasing. A speculative explication for the fact that the base of the finger is subjected to higher deformation than its tip resides in the heterogeneity of the granular sample which is expected to be denser at the base than all along its height due to the vertical configuration of the apparatus. In these circumstances, the capillary pressure necessary to enter the throats of the granular medium is higher at the bottom of the sample than in any other place, which means that once the gas entered in the porous network, also the capillary pressure drop induced by the micro-scale invasion process and the effective

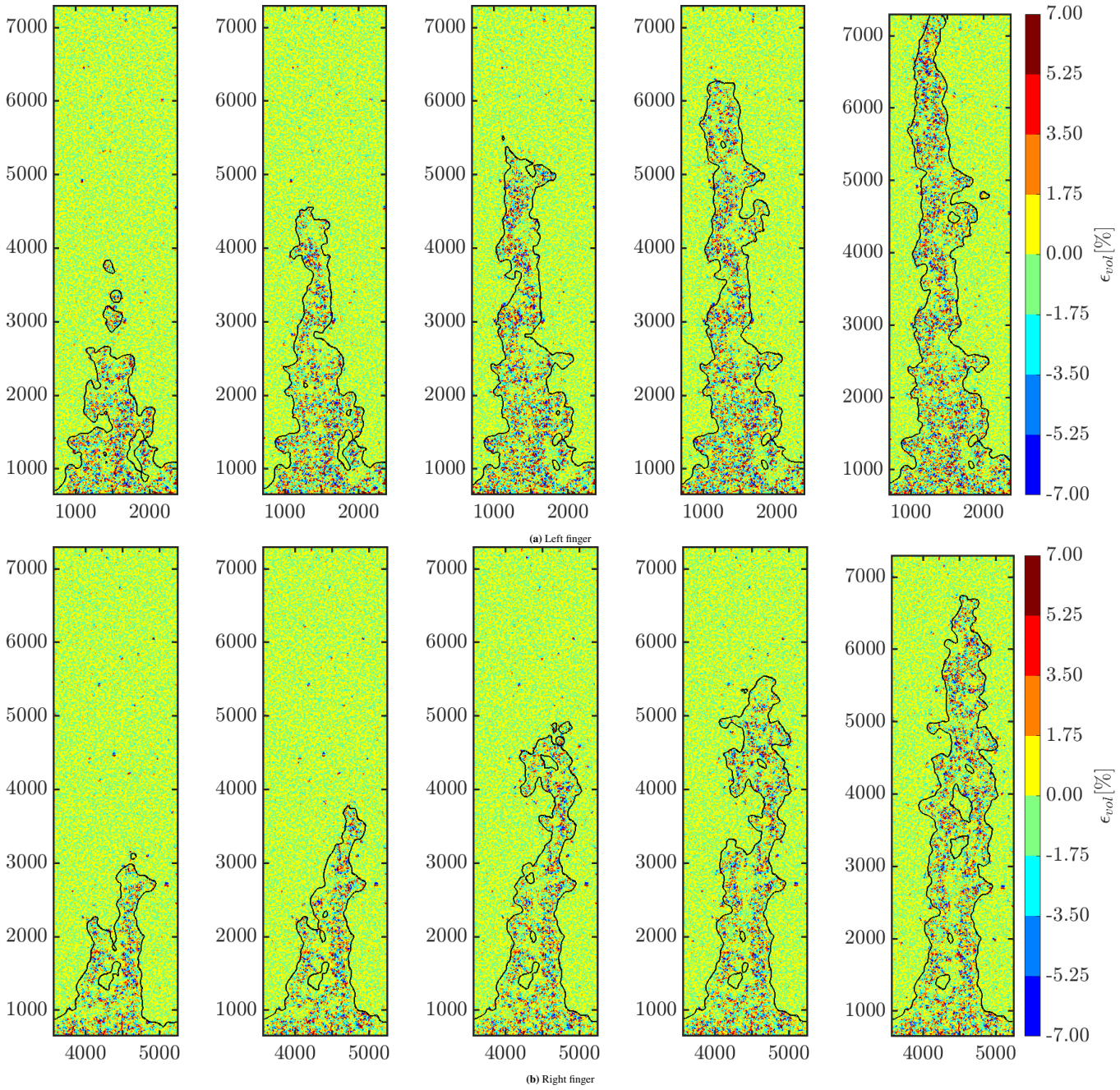

(a) Left finger

(b) Right finger

Figure 18 Volumetric strain maps for the couple of fingers detected in test (3) and evaluated at same instants. The time-steps between the maps is 0.1s.

stress release will be higher in this zone than elsewhere (see the qualitative discussion of Section 5.1). Moreover, the evolution of the intensity of the volumetric strain within the invaded zones does not always manifest as a monotonic function of time as there are groups of curves and therefore groups of transition zones interested by the formation of more than one plateau as time increases. This observation is also evident in the case of test (3) presented in Figure 23 for both fingers. This type of response reflects the fact that the air invasion process occurs with a sequence of bursts spread over a sequence of transition zones. As the set of curves provided in Figure 21b contributes to the formation of the set of curves in Figure 21a, unsurprisingly, the shape of the curves relative to the invaded zones is inherited by that of the transition zones and therefore the local evolution of deformation within each transition zone is the one behind the global response observed within the corresponding invaded zone.

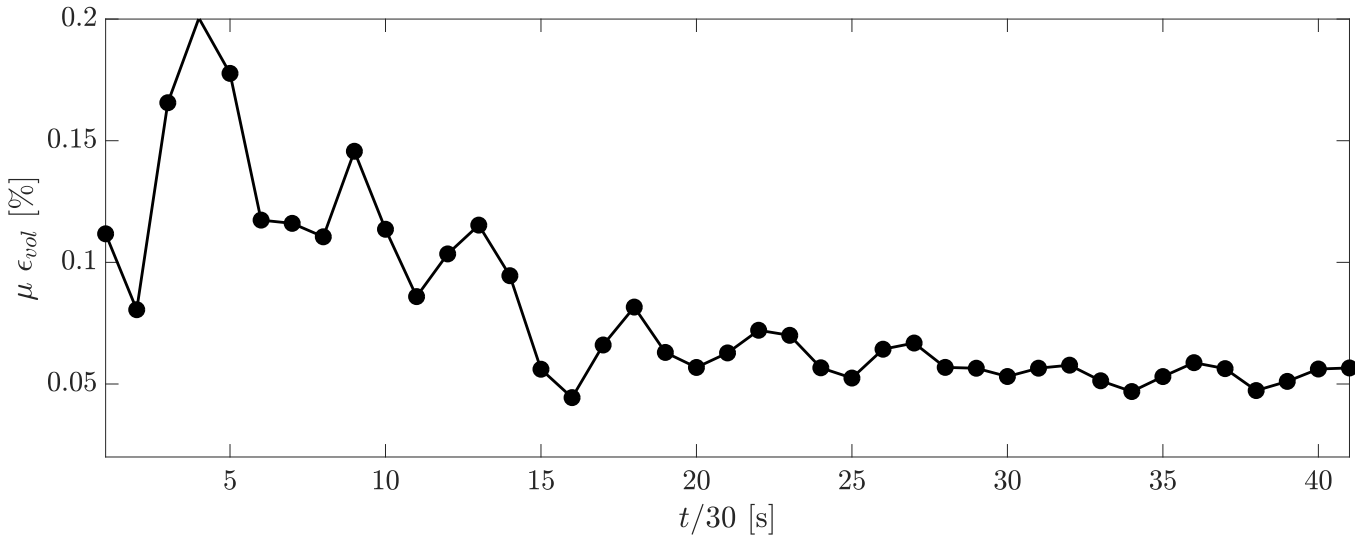

Figure 19 Evolution of the average volumetric strain within the developed finger of test (2).

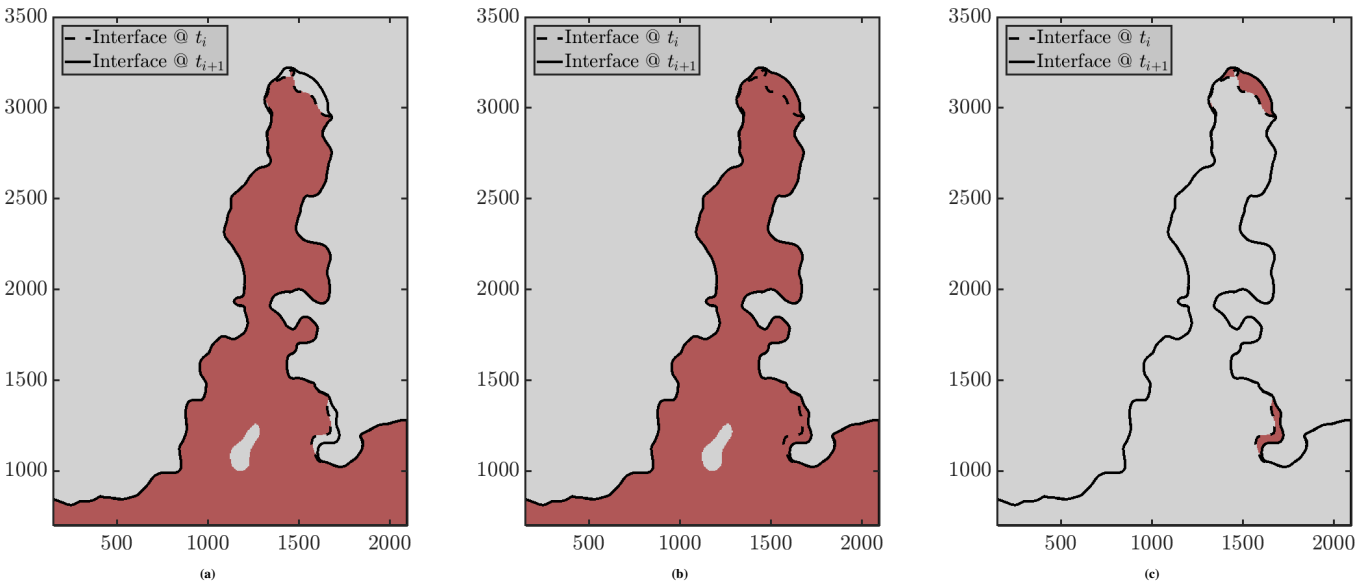

Figure 20 Example from test (1) illustrating the invaded zones for two consecutive instants vs the transition zone, in red color: (a) invaded zone at t_i, (b) invaded zone at t_{i+1} and (c) transition zone associated to t_{i+1}.

Obviously, the actual process is an irreversible one: once the deformations are generated, they are slightly amplified then remain constant over the whole process.

5.2.2 | Peak-strains description

After debriefing the coupling between the fluid flow and the generated deformation, a more local analysis concerning the element-wise response is elaborated, by searching the peak value attained during the process. The peak value being retrieved for each element within the developed finger, a pair of maps is constructed: one indicating the time at which each element has reached its peak value (see Figure 24a) and another one indicating the value of the reached peak deformation ϵ_{vol}^{peak} (see Figure 24b). These maps correspond to the drainage test (2).

Comparing Figure 22 to Figure 24a, the generation of peak deformation seems relevant to the progressive stages of the invading interface, not only in the main direction of the fluid flow -the vertical one- but also in the bifurcation branching from the body of the finger. This observation is also valid in the occurrence of a coalescence, as the one seen in test (3) and illustrated in Figure 25, through a sequence of three shots highlighting the details of this local phenomenon. During the formation of the couple of fingers in test (3), the coalescence phenomenon manifests extensively. Figure 26 summarizes the sequence of transition zones for the left and right finger in panels (a) and (c), respectively. As can be seen, the coalescence emerges once within the left finger at the height of 800 elements and twice within the right finger, the first one at the height of 600 elements (the one previously detailed

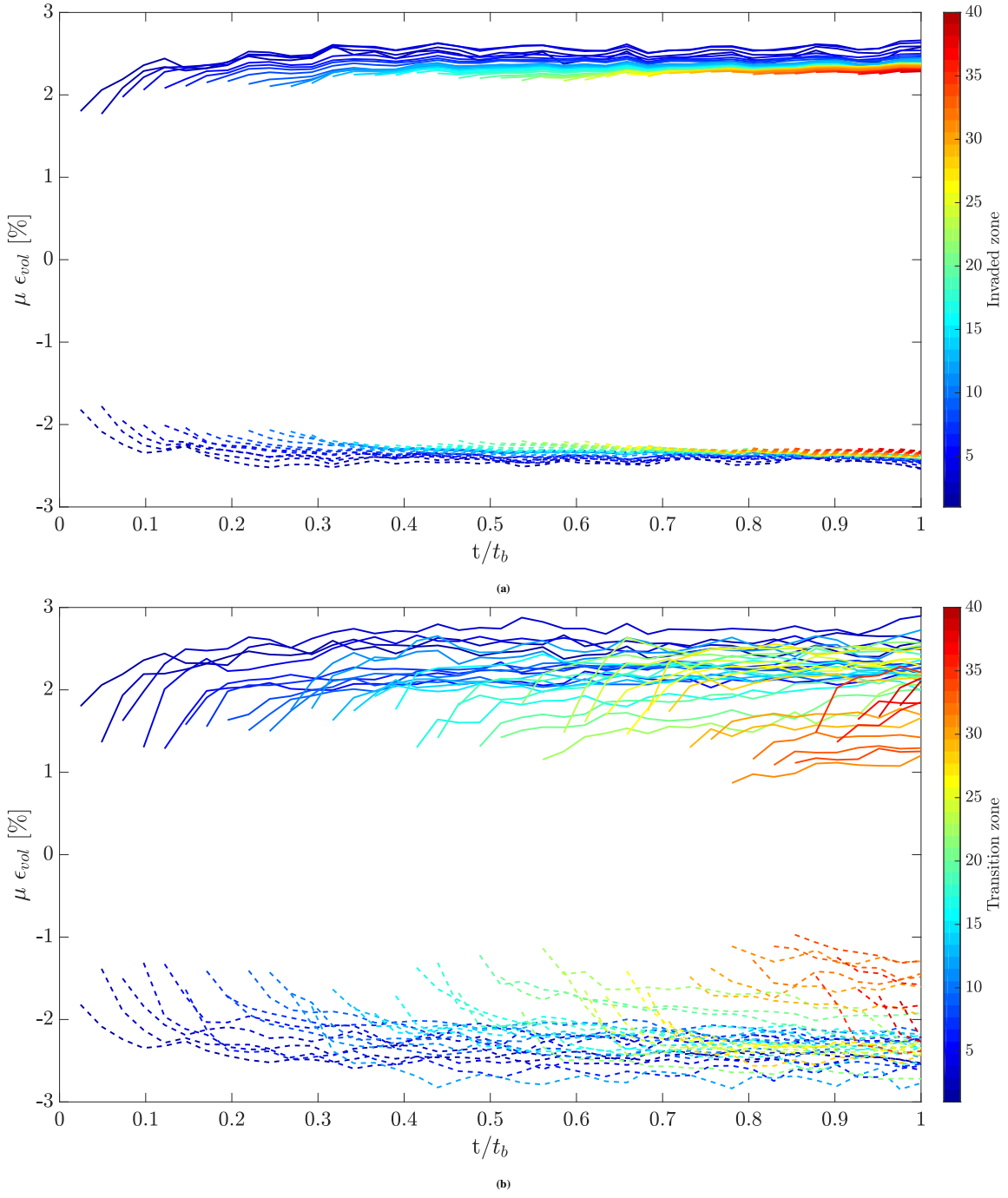

Figure 21 Evolution of the mean value of the volumetric strains during the invasion process, within the invaded zones in (a) and within the transition zones in (b), for test (2).

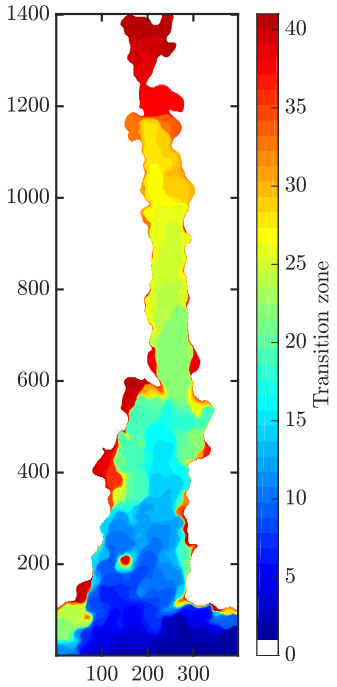

Figure 22 Element-scale map (1 element=5 pixels) showing the sequence of transition zones, acquired each 1/30 s until the breakthrough time. The white color denotes the non-invaded zone while the gradually coloured palette divides the developed finger of test (2) to distinct sequence of transition zones.

in Figure 25) and the second one at the height of 800 elements. In parallel, the maps indicating the time at which the elements have reached their peak deformation are also provided for each finger of test (3) in panels (b) and (d) of Figure 26. Comparing the maps of the peak strain and of the evolution of the gas front, one can deduce that the skeleton remodeling is driven by the gas front whether percolating in the main direction of the flow or nucleating local bifurcations/coalescences as a matter of facts for each transition zone which progressively switchs on peak strain is detected almost everywhere.

However, looking at the base of the developed finger in Figure 24a, the dark blue color is impregnated by coloured spots indicating that some elements have reached their maximum deformation at later stages, so after the nucleation of the corresponding zone. Figure 27 gives insights on this point revealing the cumulative frequency of elements that have reached their peak deformation through the drainage process, within each transition zone. As it can be seen, the transition zones at the base of the developed finger, pointed by the blue palette, confirm that the elements attain their peak deformation gradually through the process. In addition, comparing a transition zone formed at an early stage of the process (the dark blue one), versus a transition zone formed at an intermediate stage (the aqua one), the initial zone requires more time for the half of their elements to reach a peak value than the intermediate zone (around $0.36t_b$ vs $0.26t_b$, respectively).

Regardless the triggering of skeleton deformation at the moment of the invasion, the elements continue to have local fluctuations of deformation all over the process, even though at the scale of the invaded zone, the average strain witnesses an increase only over small interval of time followed by a stable mode, as can be seen in Figure 21a. Therefore, a direct question is raised: how the elements of a zone are continuously deforming and reaching their peak deformation values while the global value, averaged over a given invaded zone, does not show any increasing tendancy but in contrary a stable behavior? To answer this question, Figure 28a provides the variation of strain calculated as the difference between the peak volumetric strain and the last stage volumetric strain at the breakthrough. This reflects whether the attained peak deformations during the process are maintained all over the process or modified. As a zero $\Delta\epsilon_{vol}$ indicates that the maximal strain is attained at the breakthrough, positive or negative values of this indicator witness the fact that strains are not maintained after the passage of the gas front. For a given zone and given element, even though the elements are consecutively reaching their peak deformation, however these values are not maintained explaining the observed global response within each zone. It is worth to notice that, the map provided in Figure 28a only indicates that the record deformations are modified but it is not clear whether it is a matter of strain relaxation or an alternation of the strain sign. Therefore, a verification is conducted for each element within the finger by checking whether the sign

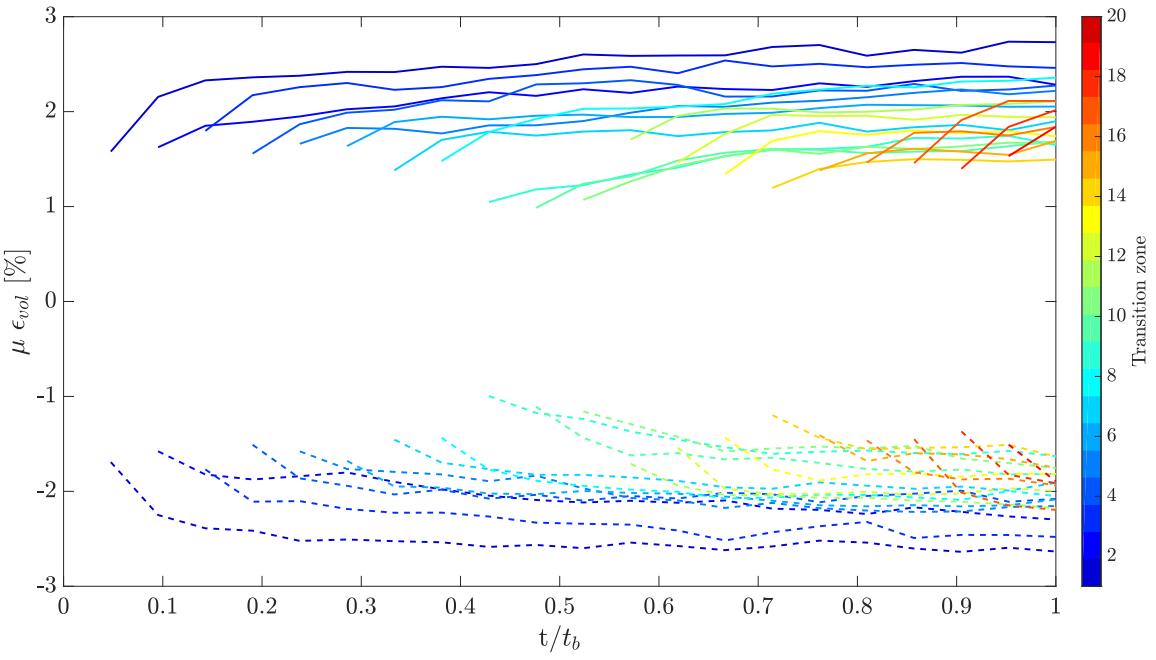

(a) Left finger

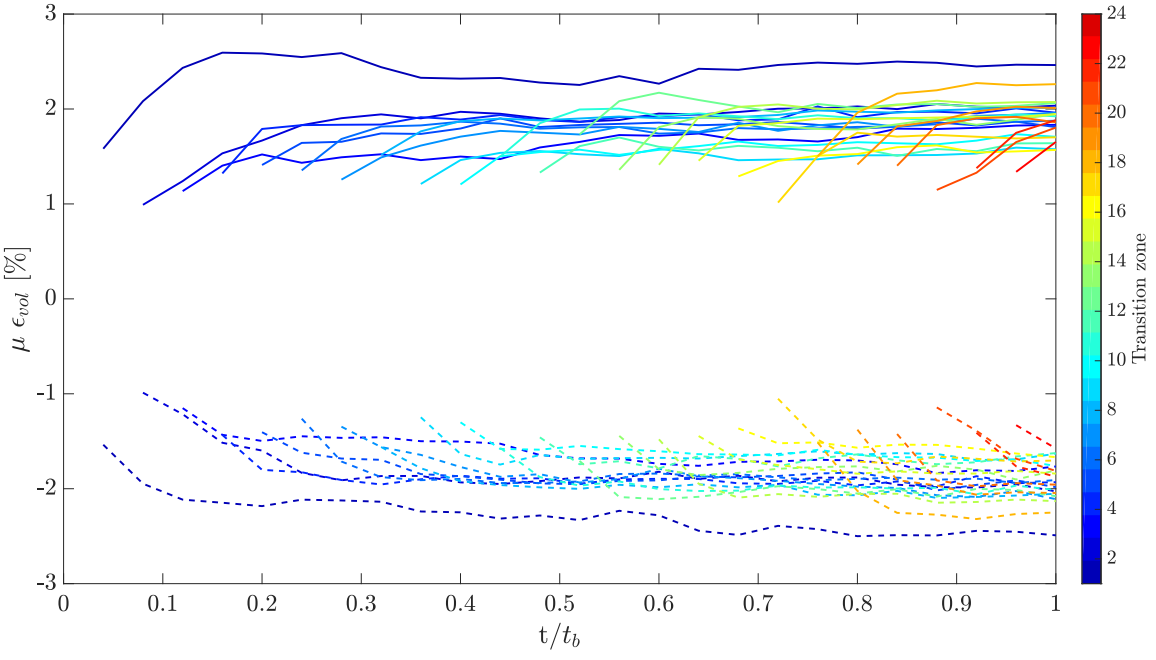

(b) Right finger

Figure 23 Evolution of the mean value of the volumetric strains during the invasion process, within the transition zones of each developed finger in test (3).

of deformation is conserved or changed between the state of peak strains and the breakthrough state. If the sign is conserved, the element witnesses a relaxation of deformation whereas if changed, the element goes from a negative volumetric strain to a positive one or inversely, but obviously with an absolute magnitude smaller than the absolute peak one. The investigation conducted for test (2) is reported in Figure 28b and Figure 28c, where in (b), the map indicates the elements that have undergone a strain softening while in (c), the map highlights the elements that have changed the sign of their deformation, considering all the elements except the one invaded at the breakthrough. Thus, a minority of elements changes their sign of deformation, while the majority of elements, after reaching their record values, experiences a decrease in the magnitude of the volumetric strain

through the process, positive strains remaining positive and the negative ones remaining negative. This behavior can be expected when working with granular materials for which part of the deformation is reversible during the process.

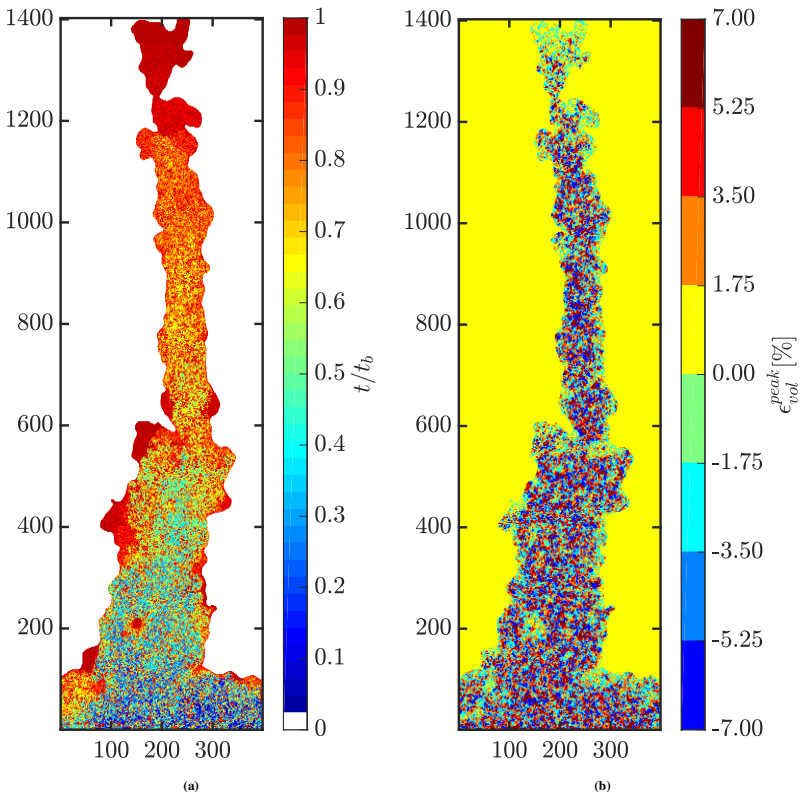

Figure 24 (a) Element-scale map describing the instant at which the elements reach their peak deformation in test (2), (b) Element-scale map describing the value of the peak deformation within the finger of test (2).

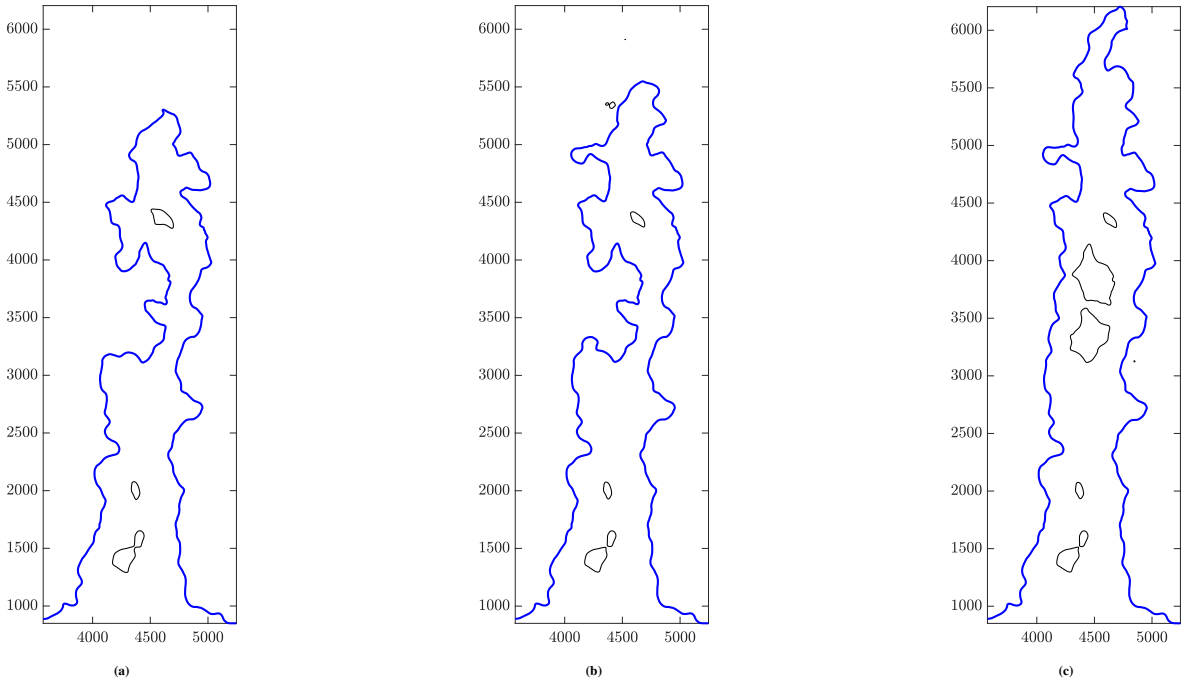

Figure 25 Consecutive stages acquired at a timestep of 1/30 s showing the coalescence of three dendritic bulges, located between 3000 and 4000 pixels along y-direction, during the propagation of the right finger of test (3).

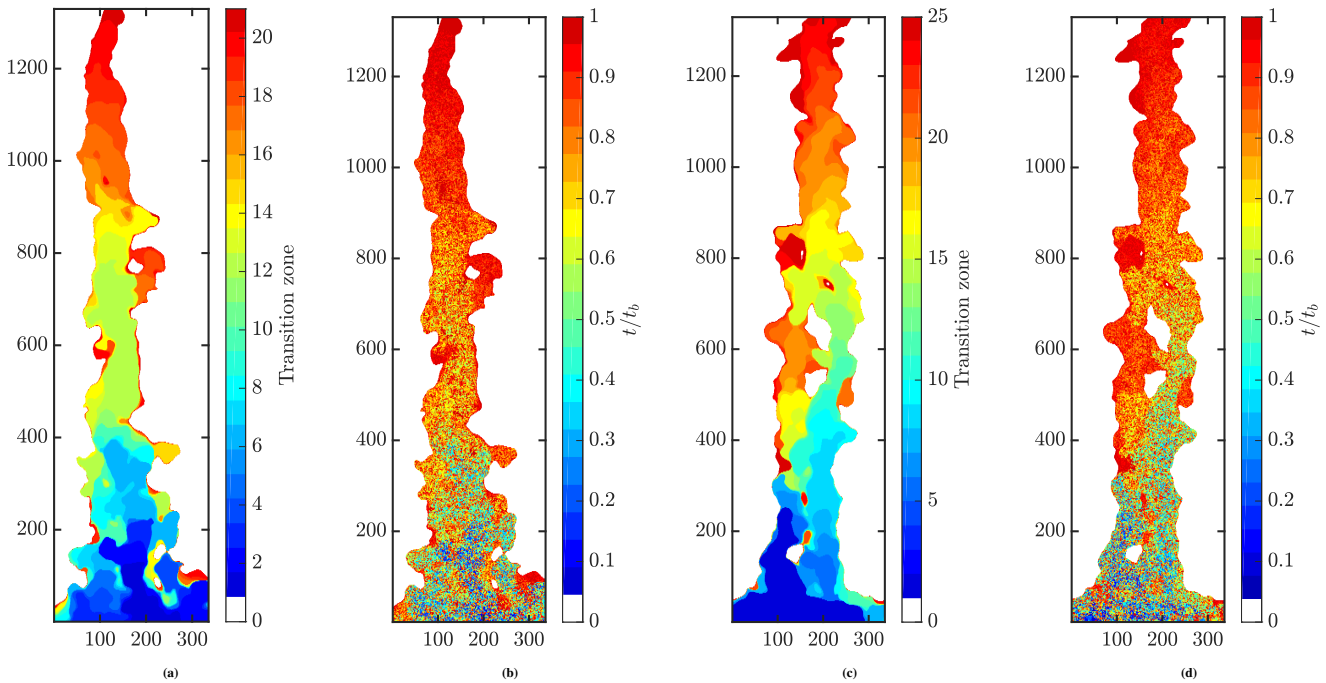

Figure 26 Comparison between the fluid flow interface and the time at which the peak deformation is reached, respectively in (a) and (b) for the left finger and in (c) and (d) for the right finger of test (3). These maps are in element scale.

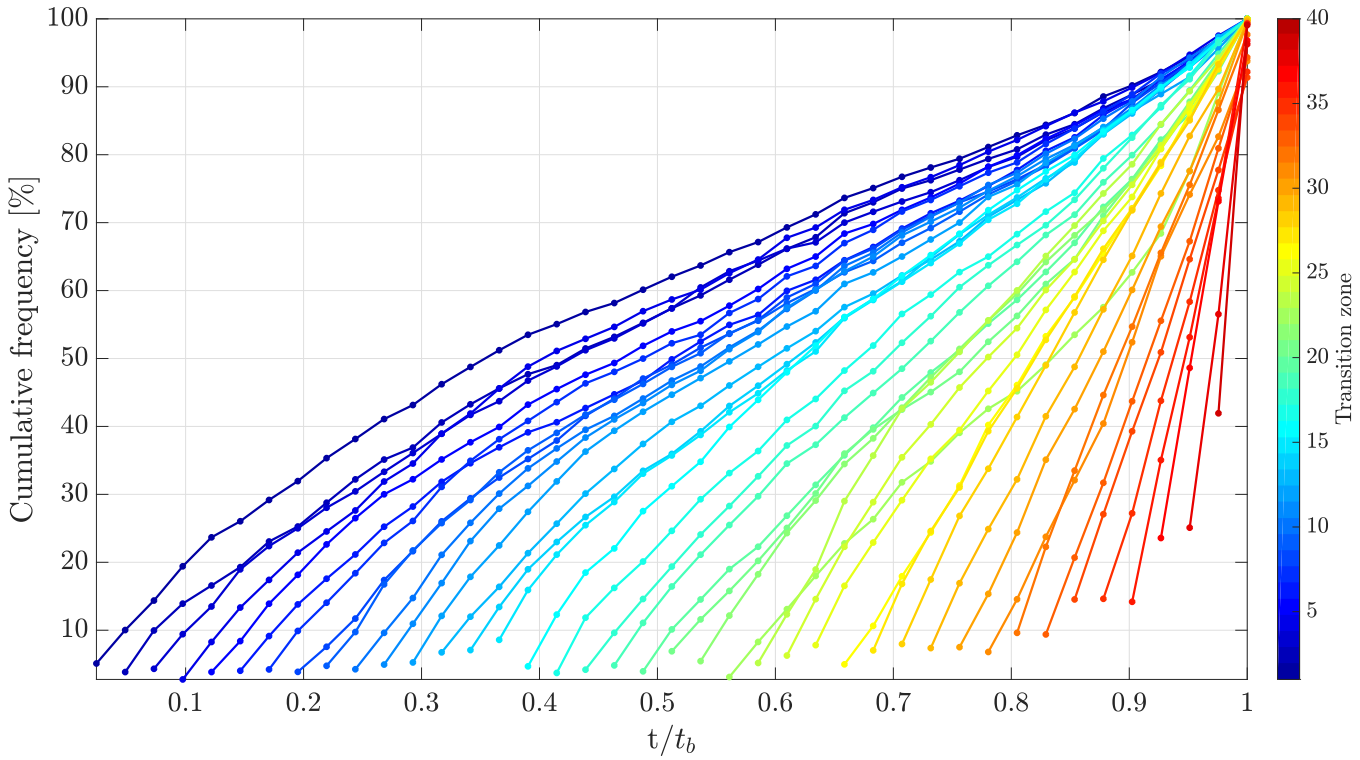

Figure 27 Set of curves, each corresponding to a transition zone and describing the cumulative frequency of elements that reached their peak deformation through time, in test (2).

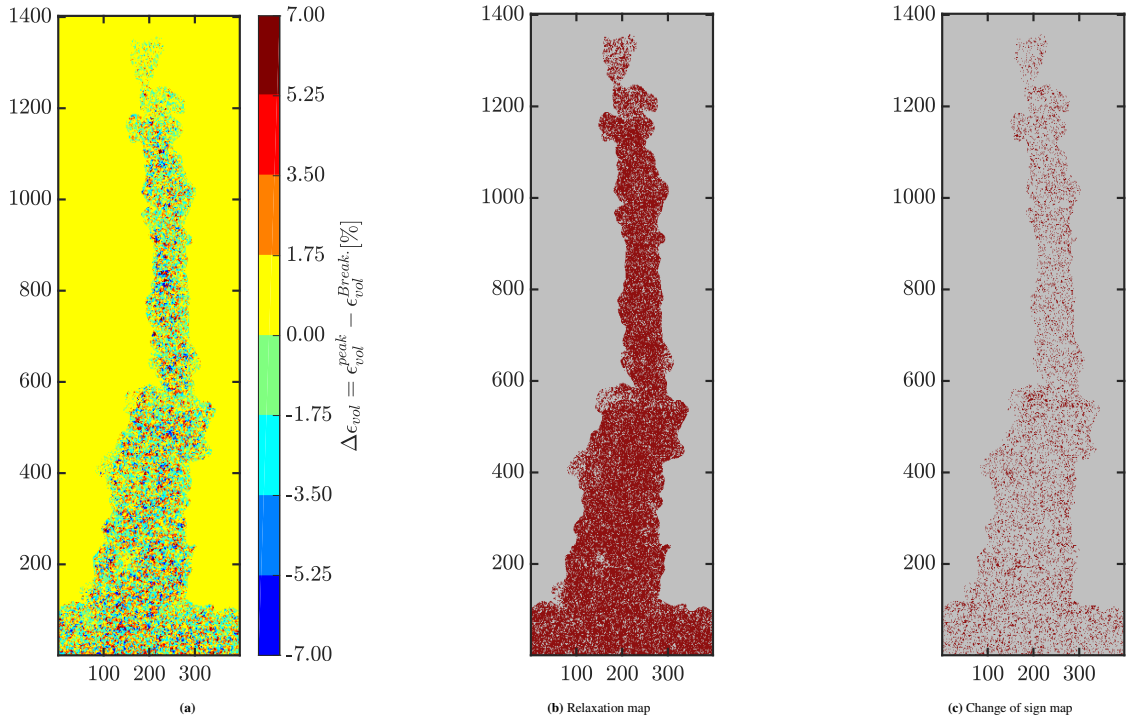

(a) **(b)** Relaxation map **(c)** Change of sign map

Figure 28 (a) Element-scale map describing the residual value between the peak deformation and the last stage deformation, detected in test (2). It is worth to point that $\Delta\epsilon_{vol}$ keeps the same sign as ϵ_{vol}^{peak} even if $\epsilon_{vol}^{Break.}$ has a different sign; (b) and (c) Qualitative maps highlighting, in dark red, the density of elements that have lost part of their peak deformation but conserved their sign in (b), and the density of elements that have changed their deformation sign in (c).

6 | CONCLUSIONS

This paper has discussed the quantification of full-field volumetric strain fields of a sand medium induced by a non-miscible biphasic flow. This latter has been triggered under hydro-mechanical loading using a biaxial machine adapted to partially saturated medium. Then via the high resolution optical system, the percolation of air-water has been filmed for three different loadings and the acquired sequences of images have supplied the DIC algorithm. A particular attention has been paid to the change of contrast induced by air infiltration and to the appropriate mesh size to be used. Then full-field volumetric strain maps have been determined and an in-depth analysis have been conducted to reveal the hidden relationship between the infiltration process and the response of the granular medium.

The obtained findings could be classified into two perspectives. From the global one, the air infiltration generates simultaneously clusters of positive and negative volumetric strains indicating the dilation and the compaction of the granular medium respectively, with an order of magnitude that largely exceeds the quantified uncertainty measurements. These volumetric strains are localized within the preferential pathway percolated by the injected fluid and their averaged value is positive indicating the dilation of the region interested by gas percolation. This result corroborates with the findings from literature concerning the macro-scale measures of volumetric strain observed in a shale sample during a drainage process, see Angeli et al.[20] and more recently Gonzalez-Blanco et al.[35]. From the local perspective, local averages of the volumetric strains over the generated invaded and transition zones are performed. They have shown that the effect of the infiltration process on the microstructure reorganization gradually decreases going from the zones at the base of the finger to the ones at the tail of the finger. Moreover, this global decreasing tendancy of the local average of volumetric strain can be characterized by a sequence of intermittent drops spread over a certain set of transition zones. On the other side, the investigation on the peak volumetric strain values reached by each element within the developed finger has led to conclude that these peak values are not maintained but undergo a relaxation or a change of sign through the drainage flow. Nevertheless, the local average volumetric strains reach a constant value indicating the irreversability of the process.

To our knowledge, the access to such local quantified information characterizing the response of the granular medium due to an unstable flow has not been yet identified in previous research work. Further investigation regarding the tracking of the advancing interface that has been essential for the present analysis, is going to be provided in future work.

ACKNOWLEDGMENTS

The authors would like to acknowledge the support of the French National Research Agency (ANR), project STOWENG (Project-ANR-18-CE05-0033) and the Carnot MERS institute, project TCIN (investigation de la sTabilité des sols dunaires sous chargement environnementaux par Corrélation d'Image Numérique).

Conflict of interest

The authors declare no potential conflict of interests.

References

[1] Dorthe Wildenschild, Adrian P Sheppard, *Advances in Water resources* **2013**, *51*, 217–246.

[2] HZ Xing, QB Zhang, CH Braithwaite, B Pan, J Zhao, *Rock Mechanics and Rock Engineering* **2017**, *50* (6), 1611–1659.

[3] Amy L Rechenmacher, Richard J Finno, *Geotechnical Testing Journal* **2004**, *27* (1), 13–22.

[4] K Liu, J Zhao, G Wu, A Maksimenko, A Haque, QB Zhang, *International Journal of Rock Mechanics and Mining Sciences* **2020**, *128*, 104260.

[5] Nicolas Lenoir, Michel Bornert, Jacques Desrues, Pierre Bésuelle, Gioacchino Viggiani, *Strain* **2007**, *43* (3), 193–205.

[6] Stephen A Hall, *Geophysical Research Letters* **2013**, *40* (11), 2613–2618.

[7] Michael A Sutton, Jean Jose Orteu, Hubert Schreier, *Image correlation for shape, motion and deformation measurements: basic concepts, theory and applications*, Springer Science & Business Media, **2009**.

[8] Stephen Hedan, Anne-Laure Fauchille, Valéry Valle, Justo Cabrera, Philippe Cosenza, *International Journal of Rock Mechanics and Mining Sciences* **2014**, *68*, 22–35.

[9] P Bésuelle, P Lanatà, *Geotechnical Testing Journal* **2016**, *39* (5), 879–890.

[10] SA Hall, N Lenoir, G Viggiani, J Desrues, P Bésuelle, in *Proceedings of the 1st Int. Symp. On Computational Geomechanics (ComGeo 1)*, **2009**, pp. 239–247.

[11] JF Labuz, S-T Dai, E Papamichos, in *International journal of rock mechanics and mining sciences & geomechanics abstracts*, Elsevier, **1996**, pp. 573–584.

[12] Ph Cosenza, M Ghoreychi, B Bazargan-Sabet, G De Marsily, *International Journal of Rock Mechanics and Mining Sciences* **1999**, *36* (4), 509–526.

[13] Roland Lenormand, *Journal of Physics: Condensed Matter* **1990**, *2* (S), SA79.

[14] Philip Geoffrey Saffman, Geoffrey Ingram Taylor, *Proceedings of the Royal Society of London. Series A. Mathematical and Physical Sciences* **1958**, *245* (1242), 312–329.

[15] Grunde Løvoll, Yves Méheust, Renaud Toussaint, Jean Schmittbuhl, Knut Jørgen Måløy, *Physical Review E* **2004**, *70* (2), 026301.

[16] Amina Islam, Sylvie Chevalier, Imen Ben Salem, Yves Bernabe, Ruben Juanes, Mohamed Sassi, *International Journal of Multiphase Flow* **2014**, *58*, 279–291.

[17] Feng Guo, Saman A Aryana, *Energies* **2019**, *12* (7), 1390.

[18] James M Campbell, Deren Ozturk, Bjørnar Sandnes, *Physical Review Applied* **2017**, *8* (6), 064029.

[19] Fredrik K Eriksen, Renaud Toussaint, Knut J Måløy, Eirik G Flekkøy, *Frontiers in Physics* **2015**, *3*, 81.

[20] Matthieu Angeli, Magnus Soldal, Elin Skurtveit, Eyvind Aker, *Energy Procedia* **2009**, *1* (1), 3351–3358.

[21] Elin Skurtveit, Eyvind Aker, Magnus Soldal, Matthieu Angeli, Zhong Wang, *Petroleum geoscience* **2012**, *18* (1), 3–15.

[22] C Chevalier, A Lindner, M Leroux, E Clément, *Journal of Non-newtonian fluid mechanics* **2009**, *158* (1-3), 63–72.

[23] Yi-Feng Chen, Dong-Sheng Wu, Shu Fang, Ran Hu, *International Journal of Heat and Mass Transfer* **2018**, *122*, 1298–1307.

[24] Kenneth H Head, et al., *Manual of soil laboratory testing. Volume 3: effective stress tests.*, John Wiley & Sons, Chichester, UK, **1998**.

[25] Rana Al Nemer, Giulio Sciarra, Julien Réthoré, *Frontiers in Physics* **2022**, *10*.

[26] Gilles Besnard, François Hild, Stéphane Roux, *Experimental mechanics* **2006**, *46*, 789–803.

[27] Jean-Charles Passieux, Robin Bouclier, *International Journal for Numerical Methods in Engineering* **2019**, *119* (6), 453–468.

[28] J Réthoré, *URL https://doi. org/10.5281/zenodo* **2018**, *1433776*.

[29] Thibaut Archer, Pierre Beauchene, Cédric Huchette, François Hild, *Measurement Science and Technology* **2019**, *31* (2), 024003.

[30] Ali Charbal, John-Eric Dufour, François Hild, M Poncelet, Ludovic Vincent, Stéphane Roux, *Experimental Mechanics* **2016**, *56* (5), 845–860.

[31] VF Sciuti, RB Canto, J Neggers, François Hild, *Optics and Lasers in Engineering* **2021**, *136*, 106316.

[32] Caroline A Schneider, Wayne S Rasband, Kevin W Eliceiri, *Nature methods* **2012**, *9* (7), 671–675.

[33] Stéphane Roux, François Hild, Hugo Leclerc, *Procedia IUTAM* **2012**, *4*, 159–168.

[34] J-E Pierré, J-C Passieux, J-N Périé, *Experimental Mechanics* **2017**, *57* (3), 443–456.

[35] Laura Gonzalez-Blanco, Enrique Romero, Paul Marschall, Séverine Levasseur, *Rock Mechanics and Rock Engineering* **2022**, *55* (3), 1159–1177.

How to cite this article: Al Nemer R., J. Réthoré, and G. Sciarra (), Quantification of localized strains induced within a granular medium by a bi-phasic flow via digital image correlation, *Strain*, .